Received: 16 January 2026 | Revised: 30 April 2026 | Accepted: 27 May 2026 | Published online: 25 June 2026

RESEARCH ARTICLE

Journal of Optics and Photonics Research
2026, Vol. 00(00) 1–24
DOI: 10.47852/bonviewJOPR62029118

BON VIEW PUBLISHING

# Film and Substrate Spectral Optical Behaviors of a Tungsten Trioxide ($WO_3$) Thin Layer Deposited on Fluorine-Doped Tin Oxide (FTO)–Coated Glass

**David Barrios-Puerto**[1,*]

[1] *Universidad Carlos III de Madrid, Spain*

**Abstract:** The effective optical constants (EOCs) of a 480 nm tungsten trioxide ($WO_3$) thin film deposited on fluorine-doped tin oxide (FTO)–coated glass were determined from collimated transmittance and reflectance measurements over the 250–2500 nm solar spectral range. The $WO_3$ EOCs were obtained by fitting the experimental spectra with the four-flux model (4FM), using previously determined optical constants of the FTO and glass layers as input parameters. This work extends previous analyses of FTO–glass bilayers to a more complex $WO_3$–FTO–glass trilayer configuration, enabling validation of the proposed framework under multilayer boundary conditions. A three-extinction matching requirement was identified from the agreement between extinction coefficients calculated from forward and backward 4FM collimated differential equations and from the EOCs under wavelength compression. In addition, a spectral limit of the optical behavior between film and substrate was consistently observed at wavelengths approximately three times the layer thickness for both FTO and $WO_3$ layers, confirming its applicability beyond bilayer systems. Thickness gradient plots of collimated light fluxes and complex electric fields revealed the transition from substrate-like incoherent behavior to film-like coherent behavior. In the coherent regime, complex electric fields were represented through wavelength-dependent Bode and Nyquist diagrams, allowing analysis of their magnitude–phase evolution within the multilayer structure. The results provide a consistent framework for determining EOCs and identifying optical regime transitions in multilayer systems, demonstrating applicability to trilayer electrochromic structures.

**Keywords:** effective optical constants, transparent conducting oxides, thin-film layers, complex electric fields, four-flux model

## 1. Introduction

In optical studies of light–matter interaction, interfaces are described by Fresnel transmission and reflection coefficients ($\tau$ & $\rho$), whereas attenuation within layers is governed by extinction. Thick layers (substrates) are analyzed through light fluxes (LFs), while thin films require complex electric fields (CEFs) to account for coherent interference effects [1]. The inverse problem of light scattering and absorption (S&A) by small particles should not take into account the size, shape, or concentration of the particles, relying exclusively on transmittance and reflectance (T&R) measurements as input parameters [2]. Radiative transfer models, such as the two-flux model (2FM) [3] and the four-flux model (4FM) [4], are commonly used to determine S&A coefficients from T&R measurements. The first 4FM solution [5] did not distinguish forward and backward (for&back) average crossing parameters or for&back, collimated and diffuse, forward scattering ratios. These distinctions were introduced in a later solution [6], based on the diffuse differential equations defined in [4] and supported by the three-extinction matching requirement (3$\varepsilon$MR). The resulting intrinsic 4FM S&A equations were subsequently used to derive the extrinsic 2FM S&A coefficients from the 2FM total differential equations [3], equalizing to the 4FM collimated plus diffuse differential equations.

Several approaches have been proposed to retrieve effective optical constants (EOCs) and thin-film thicknesses from T&R data. Recent studies have addressed the optical characterization of thin films and multilayer structures using spectroscopic techniques and radiative transfer models [7–17], including applications to transparent conductive oxides, dielectric coatings, and scattering layers [8–13]. Growing attention has been devoted to electrochromic materials and devices for smart windows and energy-efficient technologies [18–30]. However, the transition between coherent and incoherent optical behavior in thin films and its impact on determining S&A parameters across the solar spectrum remain unresolved. In this context, identifying the spectral limit of the optical behavior between film and substrate (SLOBFS) and consistently treating for&back propagation regimes are essential for a unified optical description.

Most thin-film optical characterization methods, including transfer matrix and radiative transfer models (2FM and 4FM), focus on macroscopic quantities such as T, R, and EOCs. However, the internal distribution of LFs and CEFs

***Corresponding author:** David Barrios-Puerto, Universidad Carlos III de Madrid, Spain. Email: dbarrios@ing.uc3m.es; dbarriosp76@gmail.com

in multilayer systems, together with the transition between coherent and incoherent regimes, remains poorly understood. This work extends the previous FTO–G bilayer analysis to a $WO_3$–FTO–G trilayer system, establishing a framework linking macroscopic optical measurements with internal field behavior and wavelength-dependent regime transitions.

In this work, the optical characterization of a tungsten trioxide ($WO_3$) thin layer with a thickness of 480 nm deposited on a glass substrate coated with 400 nm of fluorine-doped tin oxide (FTO) was carried out ($WO_3$–FTO–G sample). The $WO_3$ layer was fabricated following the procedure described in the work by Čolović et al. [31]. Similar $WO_3$–FTO–G samples with $WO_3$ thicknesses of 240 nm and 120 nm were combined with a nickel oxide (NiO) thin layer deposited on the same type of FTO-coated glass substrate (NiO–FTO–G), together with the electrolyte corresponding to the glass–electrolyte–glass (GEG) sample optically characterized in [6], for the fabrication of four electrochromic devices (ECDs) based on $WO_3$ and NiO [32]. These ECDs present thickness combinations of 120 nm × 120 nm, 120 nm × 240 nm, 240 nm × 120 nm, and 240 nm × 240 nm, arranged in a sandwich-type configuration of the form G–FTO–$WO_3$–E–NiO–FTO–G. Since $WO_3$ undergoes a transition from an uncolored bleached-off optical state (BOOS) to a bluish colored-on optical state (COOS), while NiO evolves from an uncolored BOOS to a brownish COOS, the complete ECD switches from an uncolored BOOS to a neutral grayish COOS. However, the $WO_3$ layer in the $WO_3$–FTO–G sample requires both an electrolyte and a counter electrode (NiO) to reach the COOS. Consequently, $WO_3$ cannot be switched to the COOS in this configuration, and only the BOOS was analyzed in the present study.

In a previous work [33], the FTO–G sample was optically characterized in the wavelength range of the solar spectrum (WRSS), and the EOCs of the FTO layer were determined and used to identify the SLOBFS at 1200 nm, corresponding to a wavelength three times larger than its thickness. The 400 nm FTO layer behaved as a substrate in the shorter-WRSS (SWRSS), from 250 nm to 1200 nm, and as a film in the longer-WRSS (LWRSS), from 1200 nm to 2500 nm. Similarly, for the $WO_3$ layer analyzed in this work, the SLOBFS was found at 1440 nm, that is, at a wavelength three times larger than its thickness. In the SWRSS, thickness gradient plots (TGPs) of the LFs were determined, whereas in the LWRSS, TGPs of the CEFs were obtained, in both cases under for&back propagation regimes, for the FTO layer of the FTO–G sample in [33] and for the $WO_3$ and FTO layers of the $WO_3$–FTO–G sample, in the present study. Analogously to the analysis of equivalent electrical circuits by electrochemical impedance spectroscopy, where frequency-dependent Bode and Nyquist diagrams of the electrical impedance are commonly obtained, Bode and Nyquist wavelength-dependent diagrams (WDD) of the CEFs were determined in the present work. This analysis was performed for both the $WO_3$ and FTO layers of the $WO_3$–FTO–G sample and, consistently with [33], also for the FTO layer of the FTO–G sample. In all cases, the diagrams were obtained within the corresponding LWRSS ranges of the FTO and $WO_3$ layers. The ultimate objective is to determine a consistent set of EOCs, together with intrinsic and extrinsic S&A parameters, for $WO_3$ and NiO layers in both their BOOS and COOS. In addition, the derivation of TGPs of magnitude, phase, and real and imaginary parts (Re&Im-P) Bode WDDs, as well as three-dimensional Nyquist WDDs, from the corresponding EOCs for the BOOS and COOS of $WO_3$ and NiO layers is also envisaged.

## 2. Experimental Details

This section presents the experimental measurements together with the wavelength-dependent configuration framework required for their interpretation. Collimated T and R of the $WO_3$–FTO–G sample were measured using the spectrometer Perkin Elmer Lambda 950 in the WRSS (250–2500 nm), with a 5 nm step. Depending on wavelength, the $WO_3$ and FTO layers may behave either as optically thin films or as optically thick substrates. This behavior defines three possible sandwich configurations for the $WO_3$–FTO–G system: film–film–substrate (FFS), substrate–film–substrate (SFS), and substrate–substrate–substrate (SSS), as illustrated in Figure 1. The transition between film and substrate regimes is governed by the SLOBFS of each layer. LFs inside substrate layers are computed from regular T ($T_{reg}$) and specular R ($R_{spe}$) measurements, whereas CEFs inside film layers are computed from the corresponding $\tau$ & $\rho$ coefficients. The for&back propagating fields are evaluated at the corresponding interfaces, located at $z = 0$, $z = \delta$, $z = \delta\delta$, and $z = \delta\delta\delta$, depending on the considered configuration. For the FFS configuration and $\lambda \geq 1440$ nm, both $WO_3$ and FTO layers are treated as films, and CEFs are computed inside each layer, while LFs are evaluated inside the G substrate. In the SFS configuration, only the FTO layer behaves as a film, whereas the $WO_3$ layer is treated as a substrate for the $SWRSS_{WO3}$. Absorption within layers is accounted for through attenuation factors $\Delta_f$ and $\Delta_s$, depending on whether the layer is treated as a film or as a substrate within the considered spectral range.

## 3. Theoretical Aspects

This section is divided into two subparts: first, the extraction of EOCs for film and substrate layers, and second, the implementation of the 4FM combined with the collimated differential equations (CDEs) and the 3εMR.

### 3.1. Complex refractive index of $WO_3$ behaving as a substrate and as a film

The formulation is based on the use of interface and layer matrices. Beginning with the complex refractive index introduced in Equation (1), $\tau$ and $\rho$ for both polarization states are derived in Equations (2)–(5). These coefficients are then employed to calculate the collimated T&R at the interfaces, denoted as (t and r), as defined in Equations (6) and (7). The interface matrix $M_{oi}^{I}$, given in Equation (8), describes light propagation from the external medium "o" (air) to the internal medium "i" (air) and is constructed using polarization-averaged S and P components. The attenuation factor due to extinction, $\Delta_s(d) = \exp(-\varepsilon^{\kappa n} \cdot dz)$, defined in Equation (9), is incorporated to build the substrate layer matrix $N_s^{I}$ in Equation (10). This formalism, summarized in Equations (1)–(10), is first applied to the FTO–G bilayer configuration [33]. For the $WO_3$–FTO–G trilayer system, the corresponding substrate matrix product is introduced in Equation (11), from which the collimated interfaces T&R of the $WO_3$ and FTO are subsequently obtained ($r_{oWO3FTOG}$, $t_{oWO3FTOG}$, $r_{GFTOWO3o}$, and $t_{GFTOWO3o}$), calculated following three different approaches associated with the FFS, SFS, and SSS configurations. For the FFS and SFS cases, the evaluation of LFs requires the determination of CEFs, as described by Equations (13)–(16). Equation (13) plays for CEFs in film layers a role analogous to that of Equation (8) for LFs in substrate

**Figure 1**

**Sandwich structures of the $WO_3$–FTO–G sample under the three considered configurations: film–film–substrate (FFS), substrate–film–substrate (SFS), and substrate–substrate–substrate (SSS). (a) for&back LFs (I & J), inside the G substrate, and (b) for&back CEFs (E & F), inside the $WO_3$ and FTO layers for FFS configuration ($\lambda \geq 1440$ nm). (c) LFs inside the $WO_3$ layer and (d) CEFs inside the FTO layer for the SFS configuration. (e) LFs inside $WO_3$ and FTO layers for the SSS configuration. Film attenuation factors $\Delta_f^{WO3}$ ($\lambda \geq 1440$ nm) and $\Delta_f^{FTO}$ ($\lambda \geq 1200$ nm), substrate attenuation factors $\Delta_s^{G}$, $\Delta_s^{WO3}$, and $\Delta_s^{FTO}$. Asterisks (*) denote arrows originating at interfaces**

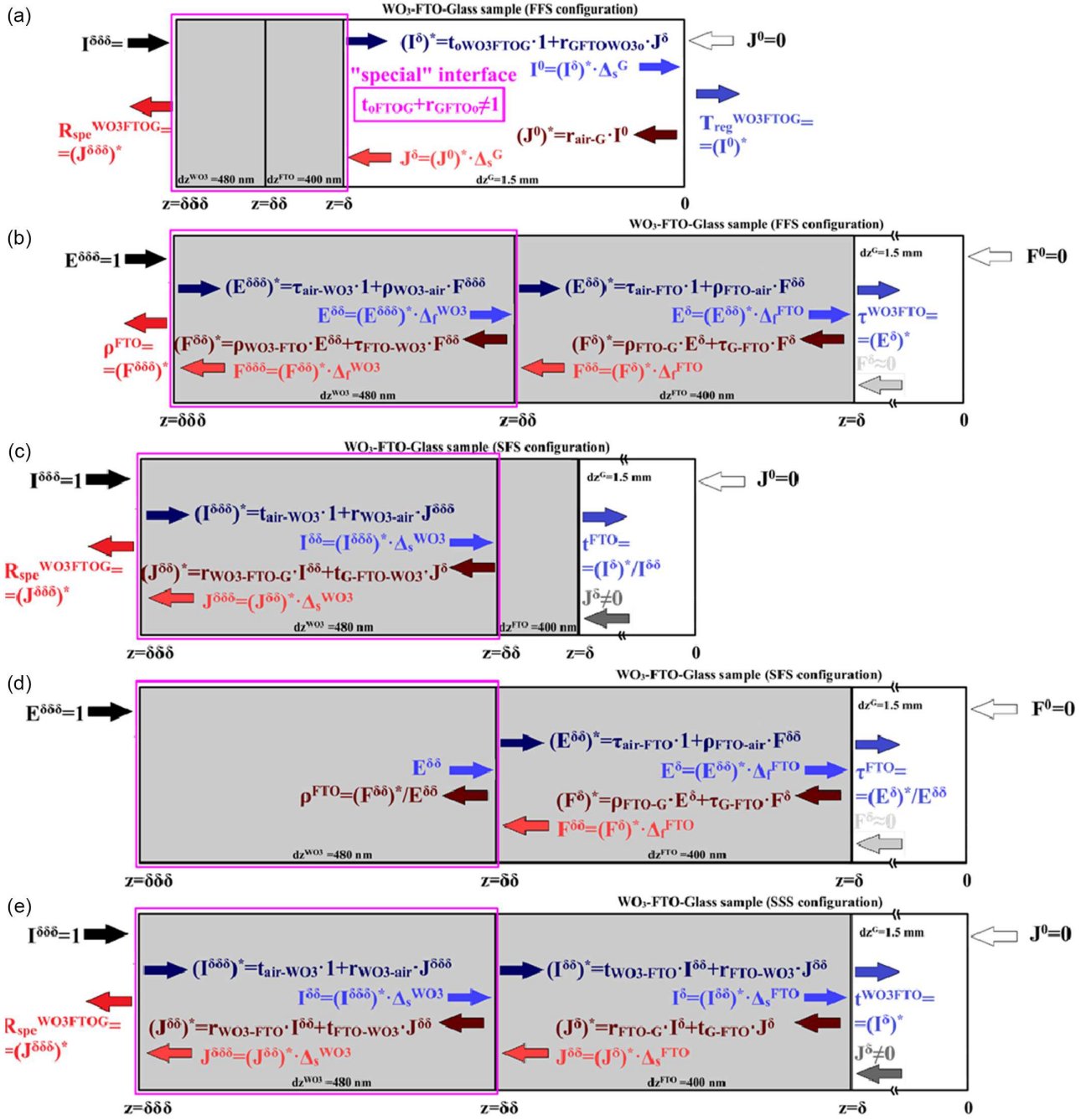

layers. The attenuation factor $\Delta_f(d)$ for $WO_3$ and FTO layers treated as films is defined in Equations (14)–(15), respectively. The wavelengths involved correspond to the effective film wavelengths ($\lambda^{WO3} = \lambda/n^{WO3}$ and $\lambda^{FTO} = \lambda/n^{FTO}$) within the LWRSS, under the condition that the thickness of the $WO_3$ and FTO layers is smaller than one third of the incident LF wavelength (i.e., 1440 nm/3 = 480 nm and 1200 nm/3 = 400 nm). The resulting film layer matrix $N_f^E$ is given in Equation (16).

$$n' = n - i\kappa \tag{1}$$

$$\tau_{oi}^S = \frac{2n_o'}{n_o' + n_i'} \tag{2}$$

$$\rho_{oi}^S = \frac{n_o' - n_i'}{n_o' + n_i'} \tag{3}$$

$$\tau_{oi}^P = \frac{2n_o'}{n_o' + n_i'} \tag{4}$$

$$\rho_{oi}^P = \frac{n_i' - n_o'}{n_o' + n_i'} \tag{5}$$

$$t_{oi}^X = Re\left(\frac{n_i'}{n_o'}\right) \cdot \left|\tau_{oi}^X\right|^2 = Re\left(\frac{n_i'}{n_o'}\right) \cdot \tau_{oi}^X \cdot \hat{\tau}_{oi}^X \tag{6}$$

$$r_{oi}^X = \left|r_{oi}^X\right|^2 = \rho_{oi}^X \cdot \hat{\rho}_{oi}^X \tag{7}$$

$$\begin{bmatrix} I_o \\ J_o \end{bmatrix} = \begin{bmatrix} \frac{1}{t_{oi}} & \frac{-r_{io}}{t_{oi}} \\ \frac{r_{oi}}{t_{oi}} & t_{io} - \frac{r_{io}r_{oi}}{t_{oi}} \end{bmatrix} \cdot \begin{bmatrix} I_i \\ J_i \end{bmatrix} = M_{oi}^I \cdot \begin{bmatrix} I_i \\ J_i \end{bmatrix} \tag{8}$$

$$\Delta_s(d) = \frac{I_2}{I_1} = exp\left(-\frac{4\pi\kappa}{\lambda_n}d\right) = exp\left(-\frac{4\pi\kappa n}{\lambda}d\right) \tag{9}$$

$$\begin{bmatrix} I_s(1) \\ J_s(1) \end{bmatrix} = \begin{bmatrix} \frac{1}{\tau_c} & 0 \\ 0 & \tau_c \end{bmatrix} \cdot \begin{bmatrix} I_s(2) \\ J_s(2) \end{bmatrix} = N_S^I \cdot \begin{bmatrix} I_s(2) \\ J_s(2) \end{bmatrix} \tag{10}$$

$$\begin{bmatrix} 1 \\ R_{cc}^{WO3FTOG} \end{bmatrix} = M_{oWO3FTOG}^I \cdot N_G^I \cdot M_{Gi}^I \cdot \begin{bmatrix} T_{cc}^{WO3FTOG} \\ 0 \end{bmatrix} \tag{11}$$

$$\begin{bmatrix} I_o \\ J_o \end{bmatrix} = \begin{bmatrix} \frac{1}{t_{oWO3FTOG}} & \frac{-r_{GFTOWO3o}}{t_{oWO3FTOG}} \\ \frac{r_{oWO3FTOG}}{t_{oWO3FTOG}} & t_{GFTOWO3o} - \frac{r_{GFTOWO3o}r_{oWO3FTOG}}{t_{oWO3FTOG}} \end{bmatrix} \cdot \begin{bmatrix} I_G \\ J_G \end{bmatrix} = M_{oWO3FTOG}^I \cdot \begin{bmatrix} I_G \\ J_G \end{bmatrix} \tag{12}$$

$$\begin{bmatrix} E_o \\ F_o \end{bmatrix} = \begin{bmatrix} \frac{1}{\tau_{oi}} & \frac{\rho_{oi}}{t_{oi}} \\ \frac{\rho_{oi}}{\tau_{oi}} & \frac{1}{\tau_{oi}} \end{bmatrix} \cdot \begin{bmatrix} E_i \\ F_i \end{bmatrix} = M_{oi}^E \cdot \begin{bmatrix} E_i \\ F_i \end{bmatrix} \tag{13}$$

$$\Delta_f^{WO3}(d) = \frac{E_2}{E_1} = exp\left(-i\frac{2\pi n}{\lambda_{WO3}}d\right) \cdot exp\left(-\frac{2\pi\kappa}{\lambda_{WO3}}d\right) \tag{14}$$

$$\Delta_f^{FTO}(d) = \frac{E_2}{E_1} = exp\left(-i\frac{2\pi n}{\lambda_{FTO}}d\right) \cdot exp\left(-\frac{2\pi\kappa}{\lambda_{FTO}}d\right) \tag{15}$$

$$\begin{bmatrix} E_f(1) \\ F_f(1) \end{bmatrix} = \begin{bmatrix} \frac{1}{\Delta_f(d)} & 0 \\ 0 & \Delta_f(d) \end{bmatrix} \cdot \begin{bmatrix} E_f(2) \\ F_f(2) \end{bmatrix} = N_f^E \cdot \begin{bmatrix} E_f(2) \\ F_f(2) \end{bmatrix} \tag{16}$$

For the FFS configuration, both $WO_3$ and FTO layers are treated as films forming a single special interface that exhibits absorption of light. The interface T&R (t and r), for for&back light propagation, associated with $M_{oWO3FTOG}{}^I$ in Equations (11)–(12) (i.e., $t_{oWO3FTOG}$, $r_{oWO3FTOG}$, $t_{GFTOWO3o}$, and $r_{GFTOWO3o}$), are obtained from the $\tau$ and $\rho$ coefficients of the individual $WO_3$ and FTO films. The resulting film matrix $M_{oWO3FTOG}{}^E$, obtained after combining interfaces and layers for CEFs, is given in Equation (17) and relates the outside air to the G substrate. Equation (18) corresponds to illumination exclusively through the interface located at $z = \delta\delta\delta$, by setting $E_o = 1$ and $F_G = 0$, and using $F_o = \rho_{oWO3FTOG}$ and $E_G = \tau_{oWO3FTOG}$. Equation (19) represents illumination solely through the interface at $z = \delta$, by setting $E_o = 0$ and $F_G = 1$, and using $E_G = \rho_{GFTOWO3o}$ and $F_o = \tau_{GFTOWO3o}$. Defining $M = M_{oWO3FTOG}{}^E = M_{oWO3}{}^E \cdot N_{WO3}{}^E \cdot M_{WO3FTO}{}^E \cdot N_{FTO}{}^E \cdot M_{FTOG}{}^E$, the $\tau$ and $\rho$ coefficients between interfaces at $z = \delta\delta\delta$ and $z = \delta$ are in Equations (20)–(27), that is, $\tau_{oWO3FTOG} = 1/M_{11}$, $\rho_{oWO3FTOG} = M_{21}/M_{11}$, $\tau_{GFTOWO3o} = (M_{11} \cdot M_{22} - M_{12} \cdot M_{21})/M_{11}$ and $\rho_{GFTOWO3o} = -M_{12}/M_{11}$. As done for standard interfaces in Equations (6) and (7), $t_{oWO3FTOG}$, $r_{oWO3FTOG}$, $t_{GFTOWO3o}$, and $r_{GFTOWO3o}$ are finally obtained using Equations (28)–(31).

$$\begin{bmatrix} E_o \\ F_o \end{bmatrix} = M_{oWO3}^E \cdot N_{WO3}^E \cdot M_{WO3FTO}^E \cdot N_{FTO}^E \cdot M_{FTOG}^E \cdot \begin{bmatrix} E_G \\ F_G \end{bmatrix} = M_{oWO3FTOG}^E \cdot \begin{bmatrix} E_G \\ F_G \end{bmatrix} \tag{17}$$

$$\begin{bmatrix} 1 \\ \rho^{oWO3FTOG} \end{bmatrix} = M_{oWO3}^E \cdot N_{WO3}^E \cdot M_{WO3FTO}^E \cdot N_{FTO}^E \cdot M_{FTOG}^E \cdot \begin{bmatrix} \tau^{oWO3FTOG} \\ 0 \end{bmatrix} = M_{oWO3FTOG}^E \cdot \begin{bmatrix} \tau^{oWO3FTOG} \\ 0 \end{bmatrix} \tag{18}$$

$$\begin{bmatrix} 0 \\ \tau^{GFTOWO3o} \end{bmatrix} = M_{GFTO}^E \cdot N_{FTO}^E \cdot M_{FTOWO3}^E \cdot N_{WO3}^E \cdot M_{WO3o}^E \cdot \begin{bmatrix} \rho^{GFTOWO3o} \\ 1 \end{bmatrix} = M_{GFTOWO3o}^E \cdot \begin{bmatrix} \rho^{GFTOWO3o} \\ 1 \end{bmatrix} \tag{19}$$

$$\tau_{oWO3FTO} = \frac{\tau_{oWO3} \cdot \tau_{WO3FTO} \cdot \Delta_f^{WO3}(d)}{1 - \rho_{WO3o} \cdot \rho_{WO3FTO} \cdot (\Delta_f^{WO3}(d))^2} \tag{20}$$

$$\rho_{oWO3FTO} = \frac{\rho_{oWO3} + \rho_{WO3FTO} \cdot (\Delta_f^{WO3}(d))^2}{1 - \rho_{WO3o} \cdot \rho_{WO3FTO} \cdot (\Delta_f^{WO3}(d))^2} \tag{21}$$

$$\tau_{FTOWO3o} = \frac{\tau_{FTOWO3} \cdot \tau_{WO3o} \cdot \Delta_f^{WO3}(d)}{1 - \rho_{WO3o} \cdot \rho_{WO3FTO} \cdot (\Delta_f^{WO3}(d))^2} \tag{22}$$

$$\rho_{FTOWO3o} = \frac{\rho_{FTOWO3} + \rho_{WO3o} \cdot (\Delta_f^{WO3}(d))^2}{1 - \rho_{WO3o} \cdot \rho_{WO3FTO} \cdot (\Delta_f^{WO3}(d))^2} \tag{23}$$

$$\tau_{oWO3FTOG} = \frac{1}{M_{11}} = \frac{\tau_{oWO3FTO} \cdot \tau_{FTOG} \cdot \Delta_f^{FTO}(d)}{1 - \rho_{FTOWO3o} \cdot \rho_{FTOG} \cdot (\Delta_f^{FTO}(d))^2} \tag{24}$$

$$\rho_{oWO3FTOG} = \frac{M_{21}}{M_{11}} = \frac{\rho_{oWO3FTO} + \rho_{FTOG} \cdot (\Delta_f^{FTO}(d))^2}{1 - \rho_{FTOWO3o} \cdot \rho_{FTOG} \cdot (\Delta_f^{FTO}(d))^2} \tag{25}$$

$$\begin{aligned} \tau_{GFTOWO3o} &= \frac{M_{11}M_{22} - M_{12}M_{21}}{M_{11}} \\ &= \frac{\tau_{GFTO} \cdot \tau_{FTOWO3o} \cdot \Delta_f^{FTO}(d)}{1 - \rho_{FTOWO3o} \cdot \rho_{FTOG} \cdot (\Delta_f^{FTO}(d))^2} \end{aligned} \tag{26}$$

$$\begin{aligned} \rho_{GFTOWO3o} &= \frac{-M_{12}}{M_{11}} \\ &= \frac{\rho_{GFTO} + \rho_{FTOWO3o} \cdot (\Delta_f^{FTO}(d))^2}{1 - \rho_{FTOWO3o} \cdot \rho_{FTOG} \cdot (\Delta_f^{FTO}(d))^2} \end{aligned} \tag{27}$$

$$t_{oWO3FTOG} = Real\left(\frac{n_G - i \cdot k_G}{n_{air}}\right) \tau_{oWO3FTOG} \cdot conj(\tau_{oWO3FTOG}) \tag{28}$$

$$r_{oWO3FTOG} = \rho_{oWO3FTOG} \cdot conj(\rho_{oWO3FTOG}) \tag{29}$$

$$t_{GFTOWO3o} = Real\left(\frac{n_{air}}{n_G - i \cdot \kappa_G}\right) \cdot \tau_{oWO3FTOG}, \cdot conj(\tau_{GFTOWO3o}) \tag{30}$$

$$r_{GFTOWO3o} = \rho_{GFTOWO3o} \cdot conj(\rho_{GFTOWO3o}) \tag{31}$$

For the SFS configuration, only the FTO layer is treated as a film acting as a special interface with absorption of light. The elements of $M_{oWO3FTOG}{}^{I}$ in Equations (11)–(12), namely, $t_{oWO3FTOG}$, $r_{oWO3FTOG}$, $t_{GFTOWO3o}$, and $r_{GFTOWO3o}$, are obtained from the $\tau$ and $\rho$ coefficients of the FTO film. The corresponding CEF matrix $M_{WO3FTOG}{}^{E}$, relating the $WO_3$ layer to the G substrate, is given in Equation (32). Equation (33) corresponds to FTO layer illumination exclusively through the interface located at $z = \delta\delta$, by setting $E_{WO3} = 1$ and $F_G = 0$, and using $F_{WO3} = \rho_{GFTOWO3}$ and $E_G = \tau_{GFTOWO3}$. Equation (34) represents FTO layer illumination solely through the interface at $z = \delta$, by setting $E_{WO3} = 0$ and $F_G = 1$, and using $E_G = \rho_{GFTOWO3}$ and $F_{WO3} = \tau_{GFTOWO3}$. Defining $W = M_{WO3FTOG}{}^{E} = M_{WO3FTO}{}^{E} \cdot N_{FTO}{}^{E} \cdot M_{FTOG}{}^{E}$, the $\tau$ and $\rho$ coefficients of the FTO layer treated as a special interface are given by $\tau_{WO3FTOG} = 1/W_{11}$, $\rho_{WO3FTOG} = W_{21}/W_{11}$, $\tau_{GFTOWO3} = (W_{11} \cdot W_{22} - W_{12} \cdot W_{21})/W_{11}$, and $\rho_{GFTOWO3} = -W_{12}/W_{11}$, in Equations (35)–(38), follow the same formal structure as Equations (20)–(27). As for standard interfaces in Equations (6)–(7), the quantities $t_{WO3FTOG}$, $r_{WO3FTOG}$, $t_{GFTOWO3}$, and $r_{GFTOWO3}$ are obtained using Equations (39)–(42), while $t_{oWO3FTOG}$, $r_{oWO3FTOG}$, $t_{GFTOWO3o}$, and $r_{GFTOWO3o}$ are computed through Equations (43)–(46). For the SSS configuration, neither CEFs nor $\tau$ and $\rho$ coefficients are required. In contrast to the SFS configuration, the quantities $t_{WO3FTOG}$, $r_{WO3FTOG}$, $t_{GFTOWO3}$, and $r_{GFTOWO3}$ are now directly computed using Equations (47)–(50), instead of Equations (39)–(42). These values are subsequently used in Equations (43)–(46) to obtain $t_{oWO3FTOG}$, $r_{oWO3FTOG}$, $t_{GFTOWO3o}$, and $r_{GFTOWO3o}$, which are finally introduced into Equations (11)–(12).

$$\begin{aligned} \begin{bmatrix} E_{WO3} \\ F_{WO3} \end{bmatrix} &= M_{WO3FTO}^{E} \cdot N_{FTO}^{E} \cdot M_{FTOG}^{E} \cdot \begin{bmatrix} E_G \\ F_G \end{bmatrix} \\ &= M_{WO3FTOG}^{E} \cdot \begin{bmatrix} E_G \\ F_G \end{bmatrix} \end{aligned} \tag{32}$$

$$\begin{aligned} \begin{bmatrix} 1 \\ \rho^{WO3FTOG} \end{bmatrix} &= M_{WO3FTO}^{E} \cdot N_{FTO}^{E} \cdot M_{FTOG}^{E} \cdot \begin{bmatrix} \tau^{WO3FTOG} \\ 0 \end{bmatrix} \\ &= M_{oWO3FTOG}^{E} \cdot \begin{bmatrix} \tau^{WO3FTOG} \\ 0 \end{bmatrix} \end{aligned} \tag{33}$$

$$\begin{aligned} \begin{bmatrix} 0 \\ \tau^{GFTOWO3} \end{bmatrix} &= M_{GFTO}^{E} \cdot N_{FTO}^{E} \cdot M_{FTOWO3}^{E} \cdot \begin{bmatrix} \rho^{GFTOWO3} \\ 1 \end{bmatrix} \\ &= M_{GFTOWO3o}^{E} \cdot \begin{bmatrix} \rho^{GFTOWO3} \\ 1 \end{bmatrix} \end{aligned} \tag{34}$$

$$\tau_{WO3FTOG} = \frac{1}{W_{11}} = \frac{\tau_{WO3FTO} \cdot \tau_{FTOG} \cdot \Delta_f^{FTO}(d)}{1 - \rho_{FTOWO3} \cdot \rho_{FTOG} \cdot (\Delta_f^{FTO}(d))^2} \tag{35}$$

$$\rho_{WO3FTOG} = \frac{W_{21}}{W_{11}} = \frac{\rho_{WO3FTO} + \rho_{FTOG} \cdot (\Delta_f^{FTO}(d))^2}{1 - \rho_{FTOWO3} \cdot \rho_{FTOG} \cdot (\Delta_f^{FTO}(d))^2} \tag{36}$$

$$\begin{aligned} \tau_{GFTOWO3} &= \frac{W_{11}W_{22} - W_{12}W_{21}}{W_{11}} \\ &= \frac{\tau_{GFTO} \cdot \tau_{FTOWO3} \cdot \Delta_f^{FTO}(d)}{1 - \rho_{FTOWO3} \cdot \rho_{FTOG} \cdot (\Delta_f^{FTO}(d))^2} \end{aligned} \tag{37}$$

$$\rho_{GFTOWO3} = \frac{-W_{12}}{W_{11}} = \frac{\rho_{GFTO} + \rho_{FTOWO3} \cdot (\Delta_f^{FTO}(d))^2}{1 - \rho_{FTOWO3} \cdot \rho_{FTOG} \cdot (\Delta_f^{FTO}(d))^2} \tag{38}$$

$$t_{WO3FTOG} = Real\left(\frac{n_G - i \cdot \kappa_G}{n_{WO3}}\right) \cdot \tau_{WO3FTOG} \cdot conj(\tau_{WO3FTOG}) \tag{39}$$

$$r_{WO3FTOG} = \rho_{WO3FTOG} \cdot conj(\rho_{WO3FTOG}) \tag{40}$$

$$t_{GFTOWO3} = Real\left(\frac{n_{WO3}}{n_G - i \cdot \kappa_G}\right) \cdot \tau_{GFTOWO3} \cdot conj(\tau_{GFTOWO3}) \tag{41}$$

$$r_{GFTOWO3} = \rho_{GFTOWO3} \cdot conj(\rho_{GFTOWO3}) \quad (42)$$

$$t_{oWO3FTOG} = \frac{t_{oWO3} \cdot t_{WO3FTOG} \cdot \Delta_s^{WO3}(d)}{1 - r_{WO3o} \cdot r_{WO3FTOG} \cdot (\Delta_s^{WO3}(d))^2} \quad (43)$$

$$r_{oWO3FTOG} = r_{oWO3} + \frac{t_{oWO3} \cdot t_{WO3o} \cdot r_{WO3FTOG} \cdot (\Delta_s^{WO3}(d))^2}{1 - r_{WO3o} \cdot r_{WO3FTOG} \cdot (\Delta_s^{WO3}(d))^2} \quad (44)$$

$$t_{GFTOWO3o} = \frac{t_{GFTOWO3} \cdot t_{WO3o} \cdot \Delta_s^{WO3}(d)}{1 - r_{WO3o} \cdot r_{WO3FTOG} \cdot (\Delta_s^{WO3}(d))^2} \quad (45)$$

$$r_{GFTOWO3o} = r_{GFTOWO3} + \frac{t_{GFTOWO3} \cdot t_{WO3FTOG} \cdot r_{WO3o} \cdot (\Delta_s^{WO3}(d))^2}{1 - r_{WO3o} \cdot r_{WO3FTOG} \cdot (\Delta_s^{WO3}(d))^2} \quad (46)$$

$$t_{WO3FTOG} = \frac{t_{WO3FTO} \cdot t_{FTOG} \cdot \Delta_s^{FTO}(d)}{1 - r_{FTOWO3} \cdot r_{FTOG} \cdot (\Delta_s^{FTO}(d))^2} \quad (47)$$

$$r_{WO3FTOG} = r_{WO3FTO} + \frac{t_{WO3FTO} \cdot t_{FTOWO3} \cdot r_{FTOG} \cdot (\Delta_s^{FTO}(d))^2}{1 - r_{FTOWO3} \cdot r_{FTOG} \cdot (\Delta_s^{FTO}(d))^2} \quad (48)$$

$$t_{GFTOWO3} = \frac{t_{GFTO} \cdot t_{FTOWO3} \cdot \Delta_s^{FTO}(d)}{1 - r_{FTOWO3} \cdot r_{FTOG} \cdot (\Delta_s^{FTO}(d))^2} \quad (49)$$

$$r_{GFTOWO3} = r_{GFTO} + \frac{t_{GFTO} \cdot t_{FTOG} \cdot r_{FTOWO3} \cdot (\Delta_s^{FTO}(d))^2}{1 - r_{FTOWO3} \cdot r_{FTOG} \cdot (\Delta_s^{FTO}(d))^2} \quad (50)$$

In addition to the coefficients associated with the $WO_3$–FTO–G stack, the terms $t_{oWO3FTOG}$, $r_{oWO3FTOG}$, $t_{GFTOWO3o}$, and $r_{GFTOWO3o}$ are also required to evaluate the exact LFs within the G substrate layer. These LFs are subsequently used to compute the ε parameters in the for&back propagation directions ($\varepsilon_G{}^I$ and $\varepsilon_G{}^J$) from the 4FM-CDEs Equations (51) and (52). Because the 3εMR is established within the G substrate of the $WO_3$–FTO–G structure, the corresponding LF-TGPs can be accurately determined for the G layers. Furthermore, when the FTO layer is considered as a substrate in the $SWRSS^{FTO}$ configuration (for $\lambda < 1200$ nm) under SSS configuration, the presence of a 3εMR at this layer enables a reliable evaluation of the LF-TGP for FTO. Similarly, a 3εMR is observed in the $WO_3$ layer when it acts as a substrate in the $SWRSS^{WO3}$ (for 1200 nm $< \lambda <$ 1440 nm) under SFS configuration. Therefore, accurate LF-TGPs can also be obtained for the $WO_3$ layer treated as a substrate for both SSS and SFS configurations. To perform these calculations, the t and r for $WO_3$, $WO_3$–FTO, FTO–G, and G must first be determined using Equations (1)–(7), corresponding to the air–$WO_3$, $WO_3$–FTO, FTO–G, and G–air interfaces.

### 3.2. Collimated differential equations of four-flux model and three-extinction matching requirement

The 4FM-CDEs symmetrical Equations (51)–(52) are applied to the for&back LFs. From these expressions, the for&back $\varepsilon_G{}^I$ and $\varepsilon_G{}^J$ were achieved for the G substrate layer of the $WO_3$–FTO–G sample in this work, as well as for the FTO–G and G samples reported in the work by Barrios-Puerto [33], by means of the attenuation factor $\Delta_s{}^G(d)$ observed in Figure 1(a), for the FFS configuration (and also applied to the SFS and SSS configurations). The 3εMR in the G layer implies that $\varepsilon_G{}^I = \varepsilon_G{}^J = \varepsilon_G{}^{\kappa n}$. Similarly, the 4FM-CDE Equations (53)–(54) are symmetrical equations used to determine the forward $\varepsilon_{FTO}{}^I$ and the backward $\varepsilon_{FTO}{}^J$ of the inner FTO layer when it is treated as a substrate, at the $SWRSS^{FTO}$, as illustrated in Figure 1(e), exclusively for the SSS configuration. The corresponding 3εMR of the FTO layer leads to $\varepsilon_{FTO}{}^I = \varepsilon_{FTO}{}^J = \varepsilon_{FTO}{}^{\kappa n}$. The 3εMR results for the G and FTO layers are not explicitly plotted in this work but can be found in the work by Barrios-Puerto [33]. In addition, the 4FM-CDEs symmetrical Equations (55)–(56) are employed to determine the for&back LFs of the inner $WO_3$ layer when it behaves as a substrate, at the $SWRSS^{WO3}$, as shown in Figures 1(c) and 1(e), for the SFS and SSS configurations, respectively.

$$\frac{dI}{dz} = \frac{\left(I^{\delta}\right)^* - \left(I^0\right)}{dz^G} = \varepsilon_G^I \cdot \left(I^{\delta}\right)^* \quad (51)$$

$$\frac{dJ}{dz} = \frac{\left(J^{\delta}\right) - \left(J^0\right)^*}{dz^G} = -\varepsilon_G^J \cdot J^{\delta} \quad (52)$$

$$\frac{dI}{dz} = \frac{\left(I^{\delta\delta}\right)^* - \left(I^{\delta}\right)}{dz^{FTO}} = \varepsilon_{FTO}^I \cdot \left(I^{\delta\delta}\right)^* \quad (53)$$

$$\frac{dJ}{dz} = \frac{\left(J^{\delta\delta}\right) - \left(J^{\delta}\right)^*}{dz^{FTO}} = -\varepsilon_{FTO}^J \cdot J^{\delta\delta} \quad (54)$$

$$\frac{dI}{dz} = \frac{\left(I^{\delta\delta\delta}\right)^* - \left(I^{\delta\delta}\right)}{dz^{WO3}} = \varepsilon_{WO3}^I \cdot \left(I^{\delta\delta\delta}\right)^* \quad (55)$$

$$\frac{dJ}{dz} = \frac{\left(J^{\delta\delta\delta}\right) - \left(J^{\delta\delta}\right)^*}{dz^{WO3}} = -\varepsilon_{WO3}^J \cdot J^{\delta\delta\delta} \quad (56)$$

In Figure 1(a), under the FFS configuration, the forward LF at the interface located at $z = \delta$, denoted as $(I^{\delta})^*$, is evaluated for the air–$WO_3$–FTO–G special interface, while the backward LF at $z = 0$, $(J^0)^*$, corresponds to the G–air standard interface. The set $(I^{\delta})^*$, $(J^0)^*$, $I^0$, and $J^{\delta}$, representing the LFs at the boundaries of the G layer, was obtained using Equations (57)–(60) and subsequently introduced into Equations (51)–(52) to determine $\varepsilon_G{}^I$ and $\varepsilon_G{}^J$. The parameters $t_{oWO3FTOG}$ and $r_{GFTOWO3o}$ were computed using Equations (28) and (31) for the FFS configuration; Equations (43) and (46), together with Equations (39)–(42), for the SFS configuration; and Equations (43) and (46), combined with Equations (47)–(50), for the SSS configuration. The resulting values of $\varepsilon_G{}^I$ and $\varepsilon_G{}^J$ coincide with $\varepsilon_G{}^{\kappa n}$ because of the 3εMR previously reported in work by Barrios-Puerto [33] from $T_{reg}$ and $R_{spe}$ measurements performed on the G substrate and the FTO–G

bilayer. Applying the same procedure to the $WO_3$–FTO–G sample, the 3εMR was likewise obtained for the glass substrate layer under the three configurations considered, namely, FFS, SFS, and SSS. When the FTO layer is treated as a film, the forward LF at $z = \delta\delta$, $(I^{\delta\delta})^*$, is evaluated for the air–$WO_3$–FTO special interface in Figure 1(c) under the SFS configuration, and for the $WO_3$–FTO standard interface in Figure 1(e) under the SSS configuration, when the FTO layer is treated as a substrate. The backward LF at $z = \delta$, $(J^{\delta})^*$, corresponds to the G–FTO standard interface in both cases. The set $(I^{\delta\delta})^*$, $(J^{\delta})^*$ $I^{\delta}$, and $J^{\delta\delta}$, defining the LFs at the boundaries of the FTO layer, was obtained using Equations (61)–(64) and introduced into Equations (53)–(54) to determine $\varepsilon_{FTO}{}^{I}$ and $\varepsilon_{FTO}{}^{J}$. In this case, the coefficients $t_{oWO3FTO}$ and $r_{FTOWO3o}$ appearing in Equation (61) were computed using Equations (39) and (42) for the SFS configuration and Equations (47) and (50) for the SSS configuration. For the $WO_3$ layer considered as a substrate, the forward LF at $z = \delta\delta\delta$, $(I^{\delta\delta\delta})^*$, corresponds to the air–$WO_3$ standard interface in both Figures 1(c) and 1(e), under the SFS and SSS configurations, respectively. The backward LF at $z = \delta\delta$, $(J^{\delta\delta})^*$, is associated with the G–FTO–$WO_3$ special interface in Figure 1(c) for the SFS configuration and with the FTO–$WO_3$ standard interface in Figure 1(e) for the SSS configuration. The set $(I^{\delta\delta\delta})^*$, $(J^{\delta\delta})^*$, $I^{\delta\delta}$ and $J^{\delta\delta\delta}$, corresponding to the boundaries of the $WO_3$ layer, was obtained using Equations (65)–(68) and introduced into Equations (55)–(56) to determine $\varepsilon_{WO3}{}^{I}$ and $\varepsilon_{WO3}{}^{J}$. Since illumination was applied exclusively through the top interface at $z = \delta\delta\delta$, asterisked LFs represent the sum of transmitted and reflected contributions at this interface, whereas at the bottom interface ($z = 0$), only the reflected component is considered. For standard interfaces, the relations $t + r = 1$ hold and both coefficients are identical for for&back light senses. In contrast, for special interfaces $t + r < 1$, with $t$ remaining identical for both senses while $r$ differs.

$$\left(I^{\delta}\right)^{*} = t_{oWO3FTOG} \cdot 1 + r_{GFTOWO3o} \cdot J^{\delta} \tag{57}$$

$$\left(J^{0}\right)^{*} = r_{G} \cdot I^{0} \tag{58}$$

$$I^{0} = \frac{T_{reg}^{WO3FTOG}}{t_{G}} \tag{59}$$

$$J^{\delta} = \frac{R_{spe}^{WO3FTOG} - r_{oWO3FTOG}}{t_{GFTOWO3o}} \tag{60}$$

$$\left(I^{\delta\delta}\right)^{*} = t_{oWO3FTO} \cdot 1 + r_{FTOWO3o} \cdot J^{\delta\delta} \tag{61}$$

$$\left(J^{\delta}\right)^{*} = t_{GFTO} \cdot J^{\delta} + r_{FTOG} \cdot I^{\delta} \tag{62}$$

$$I^{\delta} = \left(I^{\delta}\right)^{*} \cdot \Delta_{s}^{FTO} \tag{63}$$

$$J^{\delta\delta} = \left(J^{\delta}\right)^{*} \cdot \Delta_{s}^{FTO} \tag{64}$$

$$\left(I^{\delta\delta\delta}\right)^{*} = t_{oWO3} \cdot 1 + r_{WO3o} \cdot J^{\delta\delta\delta} \tag{65}$$

$$\left(J^{\delta\delta}\right)^{*} = t_{FTOWO3} \cdot J^{\delta\delta} + r_{WO3FTO} \cdot I^{\delta\delta} \tag{66}$$

$$I^{\delta\delta} = \left(I^{\delta\delta}\right)^{*} \cdot \Delta_{s}^{WO3} \tag{67}$$

$$J^{\delta\delta\delta} = \frac{R_{spe}^{WO3FTOG} - r_{oWO3}}{t_{WO3o}} \tag{68}$$

For the G substrate, $\varepsilon_{G}{}^{I}$ and $\varepsilon_{G}{}^{J}$ were evaluated using Equations (51) and (52), originally derived in work by Barrios-Puerto [33], and were found to coincide with the parameter $\varepsilon_{G}{}^{\kappa n}$ defined in Equation (69). The attenuation of the LFs within the G layer is described by Equation (9) through the factor $\Delta_{s}{}^{G}(d) = \exp(-\varepsilon_{G}{}^{\kappa n} \cdot dz^{G})$. An analogous procedure was applied to the FTO layer when treated as a substrate in the $SWRSS^{FTO}$ configuration for $\lambda < 1200$ nm. In this case, $\varepsilon_{FTO}{}^{I}$ and $\varepsilon_{FTO}{}^{J}$ were obtained from Equations (53) and (54) in work by Barrios-Puerto [33], yielding the same value as $\varepsilon_{FTO}{}^{\kappa n}$ reported in Equation (70). The corresponding LFs attenuation within the FTO substrate is likewise expressed by Equation (9) as $\Delta_{s}{}^{FTO}(d) = \exp(-\varepsilon_{FTO}{}^{\kappa n} \cdot dz^{FTO})$. Similarly, for the $WO_3$ layer acting as a substrate in the $SWRSS^{WO3}$ configuration over the spectral range $\lambda < 1440$ nm, $\varepsilon_{WO3}{}^{I}$ and $\varepsilon_{WO3}{}^{J}$ were calculated using Equations (55) and (56). These coefficients were found to be identical to $\varepsilon_{WO3}{}^{\kappa n}$ as defined in Equation (71), and the attenuation of the LFs within the $WO_3$ layer is therefore given by $\Delta_{s}{}^{WO3}(d) = \exp(-\varepsilon_{WO3}{}^{\kappa n} \cdot dz^{WO3})$. From Equation (15), Equations (72) and (73) were subsequently derived to describe the Re&Im-P of the film attenuation required in the calculation of the CEF. These quantities were evaluated at four intermediate depths within the FTO layer when considered as a film, spanning from $dz_{FTO}{}^{0} = 0$ nm and $dz_{FTO}{}^{5} = 400$ nm in increments of 80 nm, allowing the determination of the FTO CEF-TGP. In an analogous manner, Equations (74) and (75) were derived from Equation (14) and evaluated at four intermediate positions within the $WO_3$ film, ranging from $dz_{WO3}{}^{0} = 0$ nm and $dz_{WO3}{}^{5} = 480$ nm with 96 nm steps, in order to obtain the $WO_3$ CEF-TGP. Accordingly, the attenuation of LFs within the G substrate follows Equation (9), where $\Delta_{s}{}^{G}(d) = \exp(-\varepsilon_{G}{}^{\kappa n} \cdot dz^{G})$. Similarly, the coefficients $\varepsilon_{FTO}{}^{I}$ and $\varepsilon_{FTO}{}^{J}$ were obtained from Equations (53) and (54) in the $SWRSS^{FTO}$ region ($\lambda < 1200$ nm), also reported in work by Barrios-Puerto [33], and coincide with $\varepsilon_{FTO}{}^{\kappa n}$ as defined in Equation (70). In this spectral range, when the FTO layer is treated as a substrate, LFs attenuation is described by Equation (9) through $\Delta_{s}{}^{FTO}(d) = \exp(-\varepsilon_{FTO}{}^{\kappa n} \cdot dz^{FTO})$. Likewise, $\varepsilon_{WO3}{}^{I}$ and $\varepsilon_{WO3}{}^{J}$ were obtained from Equations (55) and (56) in the $SWRSS^{WO3}$ region ($\lambda < 1440$ nm), leading to the same value as $\varepsilon_{WO3}{}^{\kappa n}$ in Equation (71). When the $WO_3$ layer is considered as a substrate, LFs attenuation is again governed by Equation (9), such that $\Delta_{s}{}^{WO3}(d) = \exp(-\varepsilon_{WO3}{}^{\kappa n} \cdot dz^{WO3})$. From Equation (15), Equations (72) and (73) are derived for the Re&Im-P of the film attenuation required for CEF calculations. These quantities were evaluated at four positions intermediated inside the FTO layer treated as a film, spanning from $dz_{FTO}{}^{0} = 0$ nm to $dz_{FTO}{}^{5} = 400$ nm in steps of 80 nm, enabling the construction of the FTO CEF-TGP. Analogously, Equations (74) and (75) are derived from Equation (14) for the Re&Im-P of the film attenuation associated with CEF calculations in $WO_3$. These were evaluated at four intermediate positions within the $WO_3$ layer treated as a film, between $dz_{WO3}{}^{0} = 0$ nm and $dz_{WO3}{}^{5} = 480$ nm with 96 nm increments, allowing the corresponding $WO_3$ CEF-TGP to be obtained.

$$\varepsilon_{G}^{\kappa n} = \frac{4\pi\kappa^{G}}{\lambda_{n}^{G}} = \frac{4\pi\kappa^{G} n^{G}}{\lambda} \tag{69}$$

$$\varepsilon_{FTO}^{\kappa n} = \frac{4\pi\kappa^{FTO}}{\lambda_n^{FTO}} = \frac{4\pi\kappa^{FTO} n^{FTO}}{\lambda} \tag{70}$$

$$\varepsilon_{WO3}^{\kappa n} = \frac{4\pi\kappa^{WO3}}{\lambda_n^{WO3}} = \frac{4\pi\kappa^{WO3} n^{WO3}}{\lambda} \tag{71}$$

$$\begin{aligned} Real\left[\Delta_f^{FTO}(d)\right] &= Real\left(\frac{E_2}{E_1}\right) \\ &= exp\left(-\frac{2\pi\kappa^{FTO}}{\lambda_n^{FTO}}d\right) \cdot cos\left(\frac{2\pi n^{FTO}}{\lambda_n^{FTO}}d\right) \end{aligned} \tag{72}$$

$$\begin{aligned} Imag\left[\Delta_f^{FTO}(d)\right] &= Imag\left(\frac{E_2}{E_1}\right) \\ &= exp\left(-\frac{2\pi\kappa^{FTO}}{\lambda_n^{FTO}}d\right) \cdot sin\left(\frac{2\pi n^{FTO}}{\lambda_n^{FTO}}d\right) \end{aligned} \tag{73}$$

$$\begin{aligned} Real\left[\Delta_f^{WO3}(d)\right] &= Real\left(\frac{E_2}{E_1}\right) \\ &= exp\left(-\frac{2\pi\kappa^{WO3}}{\lambda_n^{WO3}}d\right) \cdot cos\left(\frac{2\pi n^{WO3}}{\lambda_n^{WO3}}d\right) \end{aligned} \tag{74}$$

$$\begin{aligned} Imag\left[\Delta_f^{WO3}(d)\right] &= Imag\left(\frac{E_2}{E_1}\right) \\ &= exp\left(-\frac{2\pi\kappa^{WO3}}{\lambda_n^{WO3}}d\right) \cdot sin\left(\frac{2\pi n^{WO3}}{\lambda_n^{WO3}}d\right) \end{aligned} \tag{75}$$

## 4. Results and Discussion

This section is organized into three subparts. First, the LFs and CEFs evaluated at the relevant interfaces of the multilayer system are presented. Second, the LF-TGPs are analyzed for the G substrate layer, for the $WO_3$ layer treated as a substrate in the $SWRSS^{WO3}$ ($\lambda$ < 1440 nm), and for the FTO layer treated as a substrate in the $SWRSS^{FTO}$ ($\lambda$ < 1200 nm). Third, the CEF-TGPs (Bode WDD) are discussed for the $WO_3$ and FTO layers. In this last subsection, Nyquist WDD representations of the CEFs are also presented for for&back LFs. For completeness, corrected optical Nyquist WDD of the CEFs within the FTO layer of the FTO–G sample obtained in work by Barrios-Puerto [33] are also shown, allowing a direct comparison between bare FTO–G and $WO_3$-coated FTO–G systems. These diagrams are shown for the $WO_3$ and FTO layers in the spectral regions where they are treated as films, namely, the $LWRSS^{WO3}$ ($\lambda \geq 1440$ nm) and the $LWRSS^{FTO}$ ($\lambda \geq 1200$ nm), respectively.

### 4.1. LFs and CEFs at interfaces

This section is divided into two groups of eight panels each. Figure 2 presents the results associated with the LFs, whereas Figure 3 summarizes the CEFs retrieved at the relevant interfaces of the multilayer $WO_3$–FTO–G sample. Using Equation 11, an excellent agreement between reconstructed ($T_{cc}^{WO3FTOG}$ and $R_{cc}^{WO3FTOG}$) and measured ($T_{reg}^{WO3FTOG}$ and $R_{spe}^{WO3FTOG}$) is obtained in Figures 2(a) and 2(b). The experimental T&R data used in this work correspond to the $WO_3$–FTO–G sample described above and were obtained from direct spectrophotometric measurements performed at the Laboratory for Spectroscopy of Materials (National Institute of Chemistry, Ljubljana). From the EOCs of the FTO and G layers, obtained in work by Barrios-Puerto [33], the EOCs for $WO_3$ are obtained in Figures 2(c) and 2(d). These values are consistent with those reported in the literature [34–35] for $WO_3$ thin films for $\lambda$ < 1200 nm, where the refractive index typically lies between 1.8 and 2.5 depending on deposition conditions and film structure. The blue color assigned to $T_{reg}^{WO3FTOG}$ in Figure 2(a) and to $\kappa_{WO3}$ in Figure 2(d), as well as the red color used for $R_{spe}^{WO3FTOG}$ in Figure 2(b) and for $n_{WO3}$ in Figure 2(c), is intentionally chosen to emphasize the stronger physical correlation between $T_{reg}$–$\kappa$ and $R_{spe}$–n, respectively. This fitting procedure was performed by treating each thin layer ($WO_3$ and FTO) either as a substrate or as a film, depending on the considered wavelength interval. In the $WO_3$–FTO–G sample, the glass (G) layer acts as the substrate for all three configurations (FFS, SFS, and SSS), as illustrated in Figure 1. Although $T_{reg}^{WO3FTOG}$ is lower than $T_{reg}^{FTOG}$ over the entire WRSS in Figure 2(a) due to the additional extinction introduced by the $WO_3$ layer, $R_{spe}^{WO3FTOG}$ is not systematically higher than $R_{spe}^{FTOG}$ in Figure 2(b) over all $\lambda$ ranges. This behavior arises from the interplay between absorption in the $WO_3$ layer and wavelength-dependent interference effects in the multilayer system. The presence of $WO_3$ modifies the refractive-index contrast and the accumulated phase of the partial waves, leading to constructive or destructive interference that redistributes the non-transmitted energy between reflection and absorption rather than producing a monotonic increase in $R_{spe}$. A similar trend is observed when comparing $T_{reg}^{FTOG}$ with $T_{reg}^{G}$ in Figure 2(a) and $R_{spe}^{FTOG}$ with $R_{spe}^{G}$ in Figure 2(b). As shown in Figure 2(c), when $n_{WO3} < n_{FTO}$, it is satisfied that $R_{spe}^{WO3FTOG} < R_{spe}^{FTOG}$. Although $\kappa_{WO3} < \kappa_{FTO}$ over most of the WRSS, a $\lambda$ range centered around 750 nm is observed where $\kappa_{WO3} > \kappa_{FTO}$, which coincides with the same $\lambda$ range where $n_{WO3} < n_{FTO}$. Within this $\lambda$ range, $T_{reg}^{WO3FTOG} \approx T_{reg}^{FTOG}$, indicating a compensation between refractive-index contrast and absorption effects. Similarly, Figure 2(c) shows that when $n_{FTO} < n_G$, the condition $R_{spe}^{FTOG} < R_{spe}^{G}$ is fulfilled, as also observed in Figure 2(b). Although $\kappa_{FTO} > \kappa_G$ throughout the entire WRSS, the effective extinction depends on the optical path length. The interface T&R from outside air to the G substrate, crossing the $WO_3$ and FTO layers, for both for&back light senses, namely, $t^{oWO3FTOG}$, $r^{oWO3FTOG}$, $t^{GFTOWO3o}$, and $r^{GFTOWO3o}$, are shown in Figure 2(e). These quantities were computed using Equations (28)–(31) for the FFS configuration ($\lambda \geq 1440$ nm), Equations (43)–(46) combined with Equations (39)–(42) for the SFS configuration (1440 nm $\geq \lambda \geq$ 1200nm), and Equations (43)–(46) combined with Equations (47)–(50) for the SSS configuration ($\lambda$ < 1200 nm). The interface T&R from the $WO_3$ layer to the G substrate, crossing only the FTO layer, for both propagation directions, namely, $t^{WO3FTOG}$, $r^{WO3FTOG}$, $t^{GFTOWO3}$, and $r^{GFTOWO3}$, are presented in Figure 2(f). These parameters were obtained using Equations (39)–(42) for the SFS configuration and Equations (47)–(50) for the SSS configuration. Although not required for $\lambda \geq 1440$ nm to compute $t^{oWO3FTOG}$, $r^{oWO3FTOG}$, $t^{GFTOWO3o}$, and $r^{GFTOWO3o}$ in Equations (11)–(12)—which are used to determine $T_{cc}^{WO3FTOG}$ and $R_{cc}^{WO3FTOG}$— $t^{WO3FTOG}$, $r^{WO3FTOG}$, $t^{GFTOWO3}$, and $r^{GFTOWO3}$ are nevertheless shown in Figure 2(f). For consistency across the $\lambda$ range, these quantities are obtained using the SFS configuration instead of the FFS configuration. From the plots observed in Figures 2(e) and 2(f), the for&back absorptance from interface at $z = \delta\delta\delta$ to $z = \delta$ ($a_{oWO3FTOG}$ and $a_{GFTOWO3o}$, respectively) and the for&back absorptance from interface at $z = \delta\delta$ to $z = \delta$ ($a_{WO3FTOG}$ and $a_{GFTOWO3}$, respectively) are obtained in Figure 2(g). Note that the higher difference between for&back values from outside

**Figure 2**

**T&R measurements, (a) and (b). EOC: Re&Im-P EOC, (c) and (d). Interface T&R from outside air to glass substrate layer (e). Interface T&R from $WO_3$ to glass layer (f). Absorptance (g). 3$\varepsilon$MR of the $WO_3$ layer (h) for $\lambda$ < 1440 nm**

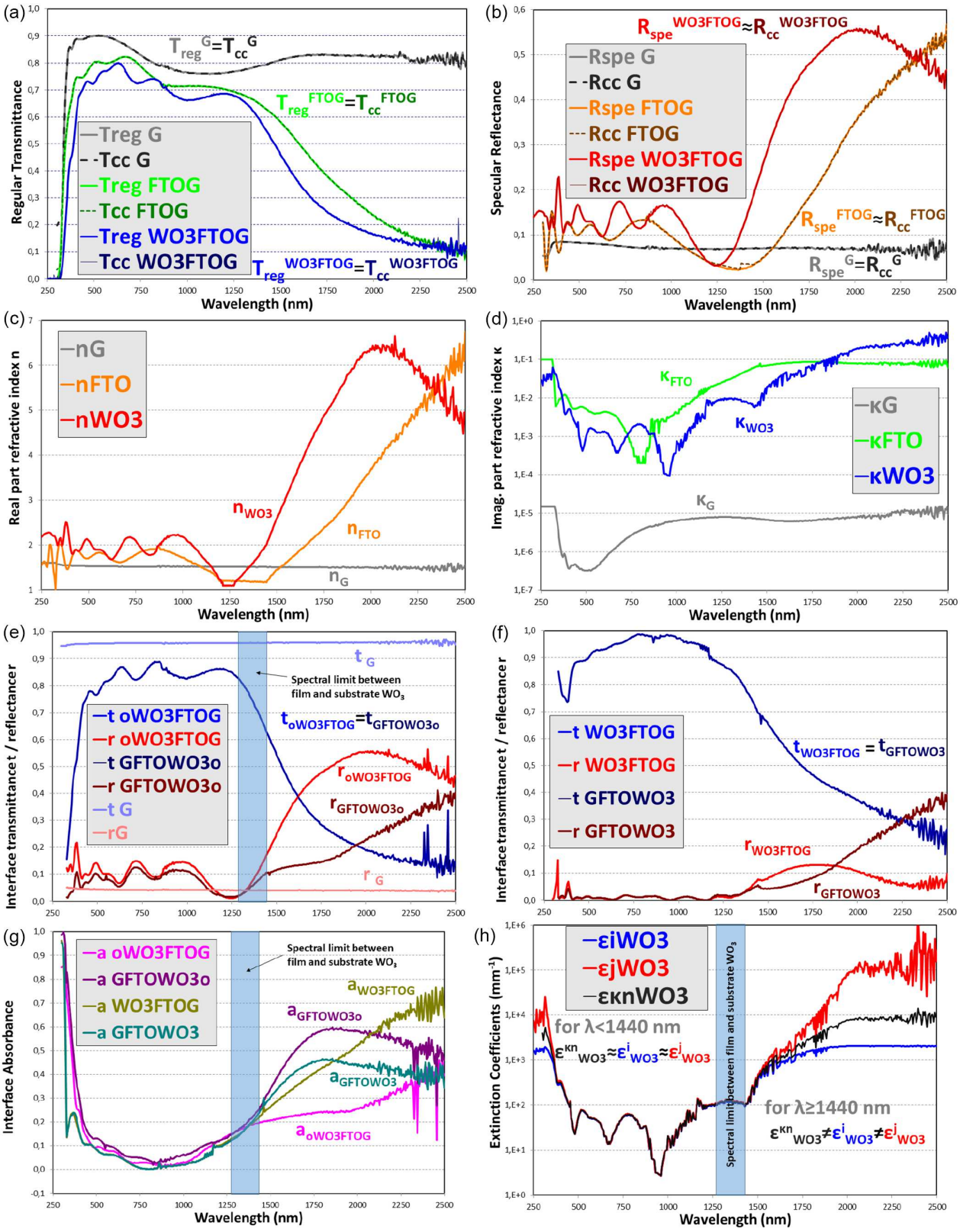

**Figure 3**

**Re&Im-P of $\tau$ & $\rho$ coefficients: For air–$WO_3$ (a), $WO_3$–G (b), and FTO–G (c) interfaces. Imaginary parts (d). Real parts (e), imaginary parts (f), magnitude (g), and phase (h) of the air–$WO_3$–FTO–G interface, for $\lambda$ > 1440 nm**

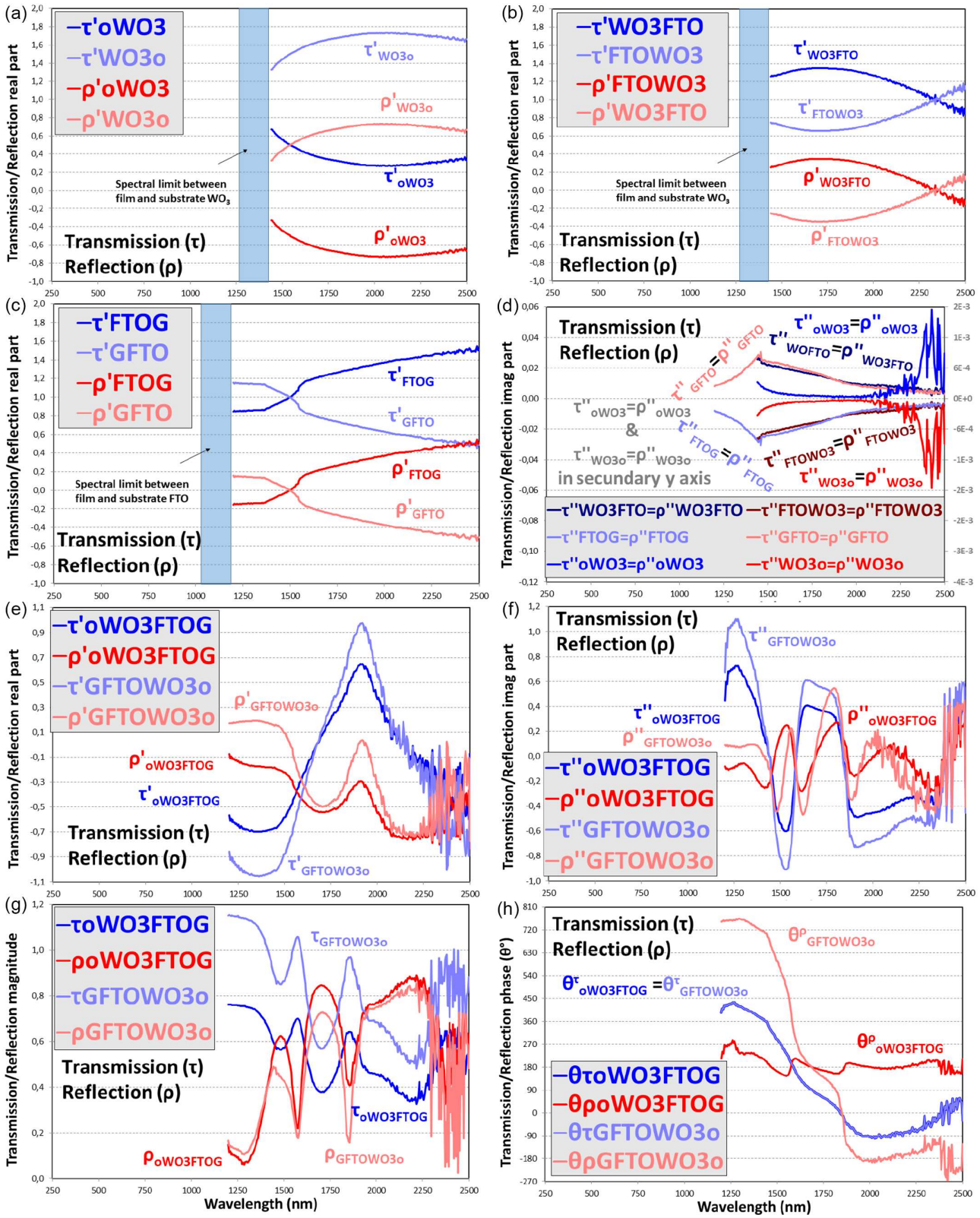

air to G substrate layer takes place for the FFS configuration. Figure 2(h) shows the 3εMR obtained for the $WO_3$ layer for the SSS and SFS configurations, in the $SWRSS^{WO3}$, and the high differences observed for the FFS configuration, in the $LWRSS^{WO3}$, where $\varepsilon^{\varkappa n}{}_{WO3}$ was obtained with Equation (71) and $\varepsilon^{I}{}_{WO3}$ and $\varepsilon^{J}{}_{WO3}$ were obtained with Equation (55)–(56). Figure 3 shows the Re&Im-P and magnitude-phase of the $\tau$ and $\rho$ coefficients for standard and special interfaces of the $WO_3$–FTO–G, depending on the $\lambda$ ranges related to each FFS and SFS configurations. The real parts of the $\tau$ and $\rho$ coefficients for the o$WO_3$ and $WO_3$-FTO standard interfaces are shown (for the $LWRSS^{WO3}$) in Figures 3(a) and 3(b), respectively, and for the FTO–G standard interface (for the $LWRSS^{FTO}$) in Figure 3(c). The imaginary parts are shown in Figure 3(d). The Re&Im-P of the $\tau$ and $\rho$ coefficients for standard interfaces were obtained by the average of the S and P polarized quantities computed with Equations (2)–(5). For the special interfaces, Equations (24)–(27) are used to determine for&back $\tau$ and $\rho$ coefficients between outside air and G substrate layer, that is, between interfaces $z = \delta\delta\delta$ and $z = \delta$ observed in Figure 1. In this way, $\tau^{oWO3FTOG}$, $\rho^{oWO3FTOG}$, $\tau^{GFTOWO3o}$, and $\rho^{GFTOWO3o}$ are plotted in Figure 3(e) for real parts, in Figure 3(f) for imaginary parts, in Figure 3(g) for magnitudes, and in Figure 3(h) for phases.

## 4.2. LFs-TGPs at $WO_3$, FTO, and G substrate layers

For the LF-TGP shown in Figures 4(a, b), four internal locations are considered within the $WO_3$ layer (480 nm thickness), treated as a substrate in the $SWRSS^{WO3}$, using a spatial step of 96 nm (with $z_{WO3}{}^0 = 0$, $z_{WO3}{}^1 = 96$ nm, $z_{WO3}{}^2 = 192$ nm, $z_{WO3}{}^3 = 288$ nm, $z_{WO3}{}^4 = 384$ nm, and $z_{WO3}{}^5 = 480$ nm). The quantities $(I^{\delta\delta\delta})^*$ and $J^{\delta\delta\delta}$ in Equations (55)−(56) are replaced by $(I^{ZZZ})^*$ and $J^{ZZZ}$ in Equations (76)−(77). Figures 4(c, d) for the FTO layer (400 nm thickness), treated as a substrate in the $SWRSS^{FTO}$, use a spatial step of 80 nm. The quantities $(I^{\delta\delta})^*$ and $J^{\delta\delta}$ in Equations (53)−(54) are replaced by $(I^{ZZ})^*$ and $J^{ZZ}$ in Equations (78)−(79). Similarly, for the G substrate, $(I^{\delta})^*$ and $J^{\delta}$ in Equations (51)−(52) are replaced by $(I^{Z})^*$ and $J^{Z}$, enabling the determination of for&back collimated LFs at internal locations within the G layer. This leads to the expressions reported in Equations (80)−(81). Accordingly, Figures 4(a)−4(b) illustrate the for&back LF-TGP within the $WO_3$ substrate layer in the $SWRSS^{WO3}$ regime ($\lambda$ < 1440 nm). Figures 4(c) and 4(d)

**Figure 4**
**LF-TGP of the $WO_3$, FTO, and G substrate layers. for&back I (a) (c) (e) and J (b) (d) (f) LFs**

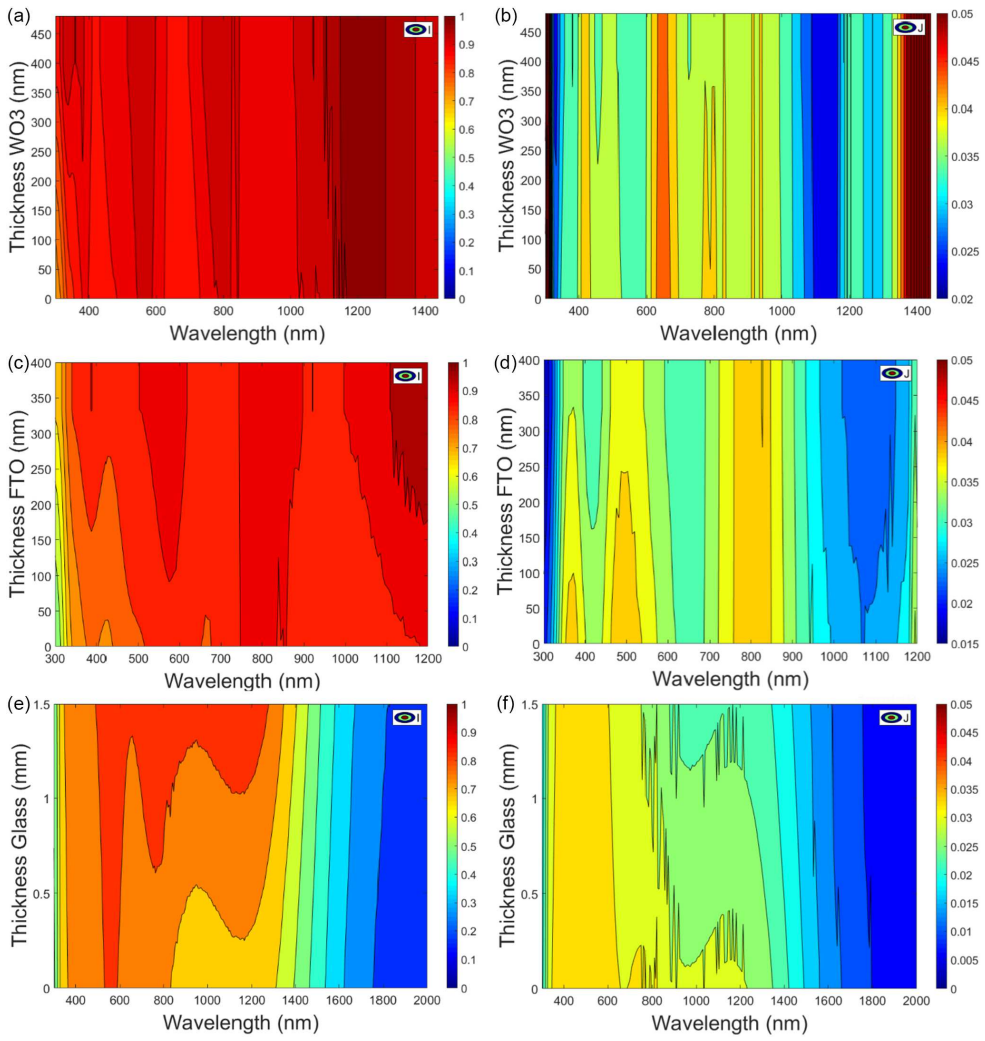

correspond to the FTO substrate layer in the SWRSS$^{FTO}$ ($\lambda$ < 1200 nm), while Figures 4(e) and 4(f) present the LFs-TGP inside the G substrate over the full WRSS (250 nm < $\lambda$ < 2500 nm).

$$\left(I^{ZZZ}\right)^{*} = \frac{I^{\delta\delta}}{1-\varepsilon^{I}_{WO3}\cdot Z} \tag{76}$$

$$J^{ZZZ} = \frac{\left(J^{\delta\delta}\right)^{*}}{1+\varepsilon^{J}_{WO3}\cdot Z} \tag{77}$$

$$\left(I^{ZZ}\right)^{*} = \frac{I^{\delta}}{1-\varepsilon^{I}_{FTO}\cdot Z} \tag{78}$$

$$J^{ZZ} = \frac{\left(J^{\delta}\right)^{*}}{1+\varepsilon^{J}_{FTO}\cdot Z} \tag{79}$$

$$\left(I^{Z}\right)^{*} = \frac{I^{0}}{1-\varepsilon^{I}_{G}\cdot Z} \tag{80}$$

$$J^{Z} = \frac{\left(J^{0}\right)^{*}}{1+\varepsilon^{J}_{G}\cdot Z} \tag{81}$$

### 4.3. CEFs-TGPs at $WO_3$ and FTO film layers

In a similar way to that of the FTO–G sample in the work by Barrios-Puerto [33], $F^{\delta}$ is computed using Equation (82) for the $WO_3$–FTO–G sample in this work (Figure 5). The complex attenuation of film layers observed in Figures 1(b) and 1(d) are calculated using Equations (83)−(84)—for the internal locations of the $WO_3$ and FTO layers when threated as substrates in Equations (76)−(81)—and used in Equations (85)−(86) to determine Re&Im-P, magnitudes, and phases of for&back CEFs inside FTO and $WO_3$ layers. Bode WDD$_S$ of the CEFs for $WO_3$ are shown in Figure 6 and their TGPs in Figure 7. Bode WDD$_S$ of the CEFs for FTO are shown in Figure 8 and their TGPs in Figure 9. Nyquist WDDs of the CEFs for $WO_3$ are shown in Figure 10. Nyquist WDDs of the CEFs for FTO of both $WO_3$FTOG and FTOG samples are shown in Figures 11 and 12, respectively. The Nyquist WDDs directly reflect the complex exponential form of the attenuation factor $\Delta_f$, where the Re&Im-P arise from the cosine and sine terms associated with phase accumulation, while the exponential term governs the damping due to extinction ($\kappa$). Consequently, the trajectories in the complex plane encode both phase evolution and attenuation of the CEFs within the layer. The circular-like trajectories observed in the Nyquist WDDs are associated with the presence of a non-zero $\kappa$, indicating that extinction within the medium governs the evolution of the CEFs in the complex plane. In contrast to Bode WDDs, the Nyquist WDDs provide a direct visualization of the imaginary and real evolution of the CEFs within the layer. In particular, the emergence of circular-like patterns reveals the extinction evolution governed by $\kappa$, which cannot be inferred from magnitude and phase plots considered separately.

$$F^{\delta} = \frac{\tau_{oWO3FTOG}\cdot\rho_{Gi}\cdot\left(\Delta^{G}_{f}(d)\right)^{2}}{1-\rho_{GFTOo}\cdot\rho_{Gi}\cdot\left(\Delta^{G}_{f}(d)\right)^{2}} \tag{82}$$

$$\Delta^{FTO}_{f}(d) = \frac{E_2}{E_1} = exp\left(-\frac{2\pi\kappa^{FTO}d}{\lambda}n^{FTO}\right)\cdot\left\{cos\left(-\frac{2\pi n^{FTO}d}{\lambda}n^{FTO}\right) + i\cdot sin\left(-\frac{2\pi n^{FTO}d}{\lambda}n^{FTO}\right)\right\} \tag{83}$$

$$\Delta^{WO3}_{f}(d) = \frac{E_2}{E_1} = exp\left(-\frac{2\pi\kappa^{WO3}d}{\lambda}n^{WO3}\right)\cdot\left\{cos\left(-\frac{2\pi n^{WO3}d}{\lambda}n^{WO3}\right) + i\cdot sin\left(-\frac{2\pi n^{WO3}d}{\lambda}n^{WO3}\right)\right\} \tag{84}$$

$$\begin{bmatrix}\left(E^{\delta\delta}\right)^{*}\\ F^{\delta\delta}\end{bmatrix} = \begin{bmatrix}\frac{1}{\Delta^{FTO}_{f}(d)} & 0\\ 0 & \Delta^{FTO}_{f}(d)\end{bmatrix}\cdot\begin{bmatrix}\left(E^{\delta}\right)\\ \left(F^{\delta}\right)^{*}\end{bmatrix} = N^{FTO}_{EF}(d)\cdot\begin{bmatrix}\left(E^{\delta}\right)\\ \left(F^{\delta}\right)^{*}\end{bmatrix} \tag{85}$$

$$\begin{bmatrix}\left(E^{\delta\delta\delta}\right)^{*}\\ F^{\delta\delta\delta}\end{bmatrix} = \begin{bmatrix}\frac{1}{\Delta^{WO3}_{f}} & 0\\ 0 & \Delta^{WO3}_{f}\end{bmatrix}\cdot\begin{bmatrix}\left(E^{\delta\delta}\right)\\ \left(F^{\delta\delta}\right)^{*}\end{bmatrix} = N^{WO3}_{EF}(d)\cdot\begin{bmatrix}\left(E^{\delta\delta}\right)\\ \left(F^{\delta\delta}\right)^{*}\end{bmatrix} \tag{86}$$

**Figure 5**
**CEF $F^{\delta}$. (a) Re&Im-P $(F')^{\delta}$ and $(F'')^{\delta}$. (b) Magnitude $|F^{\delta}|$ and $\theta$ phase (°) of $F^{\delta}$**

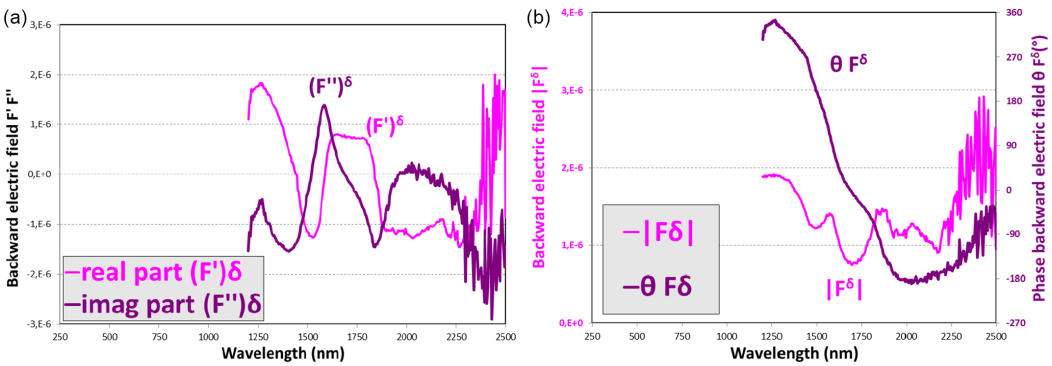

**Figure 6**
**for&back CEFs (E and J) of $WO_3$ for LWRSS$^{WO3}$. Re&Im-P: (a), (b), (c), and (d). Magnitude and phase: (e), (f), (g) and (h)**

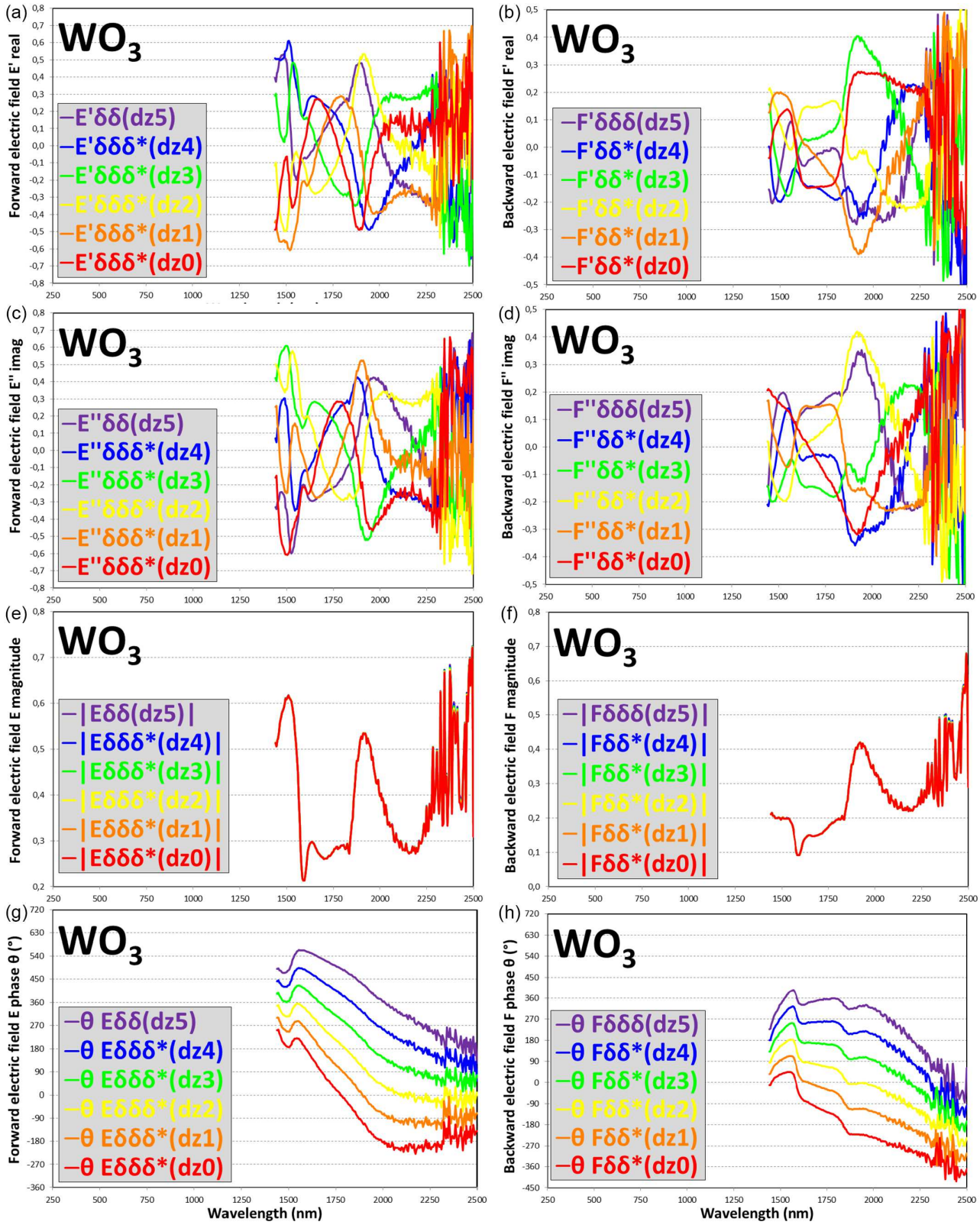

**Figure 7**
**for&back CEF-TGPs (E and F) of $WO_3$ for LWRSS$^{WO3}$. Re&Im-P: (a), (b), (c), and (d). Magnitude and phase: (e), (f), (g), and (h)**

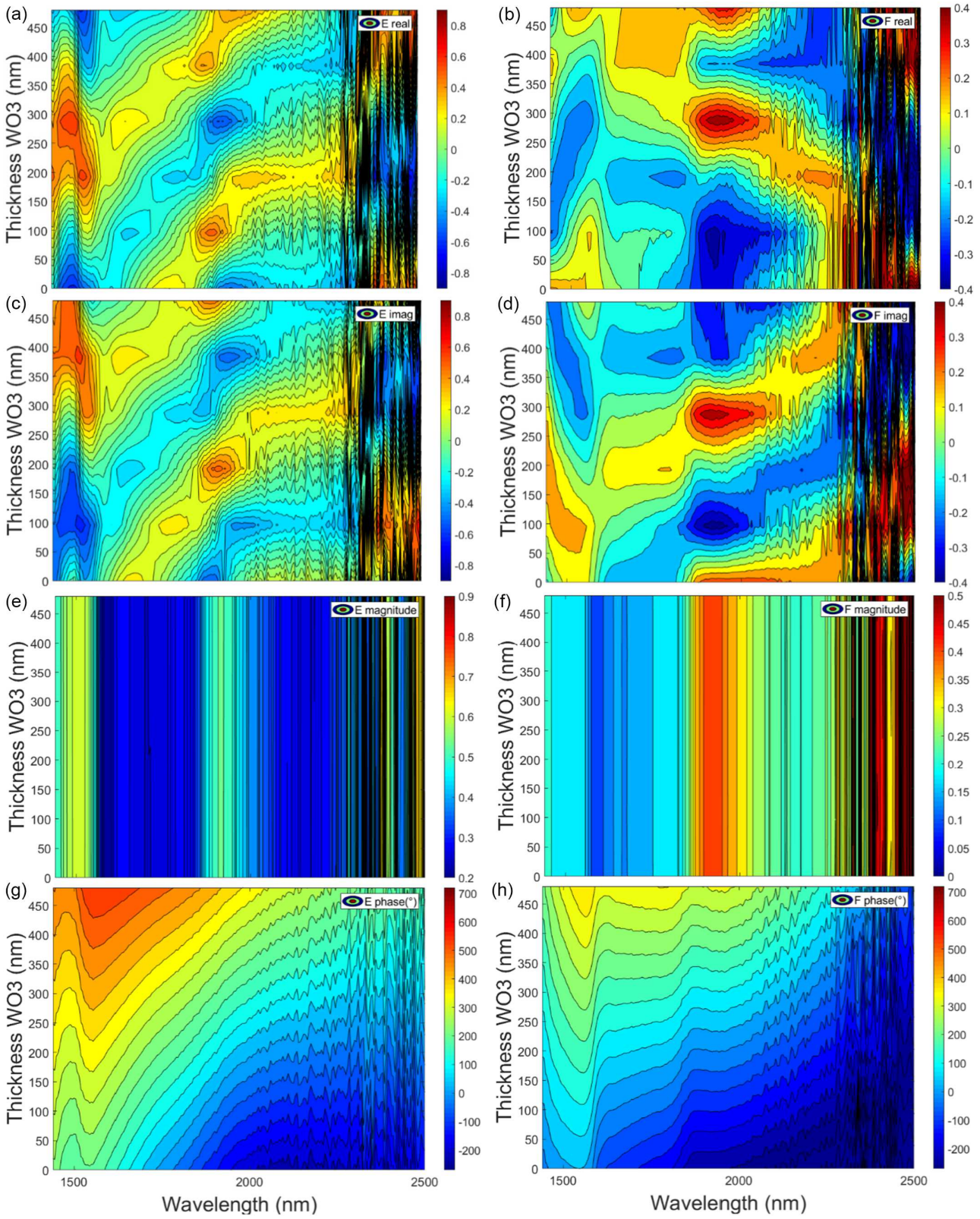

**Figure 8**
**for&back CEFs (E and J) of FTO for LWRSS$^{FTO}$. Re&Im-P: (a), (b), (c), and (d). Magnitude and phase: (e), (f), (g), and (h)**

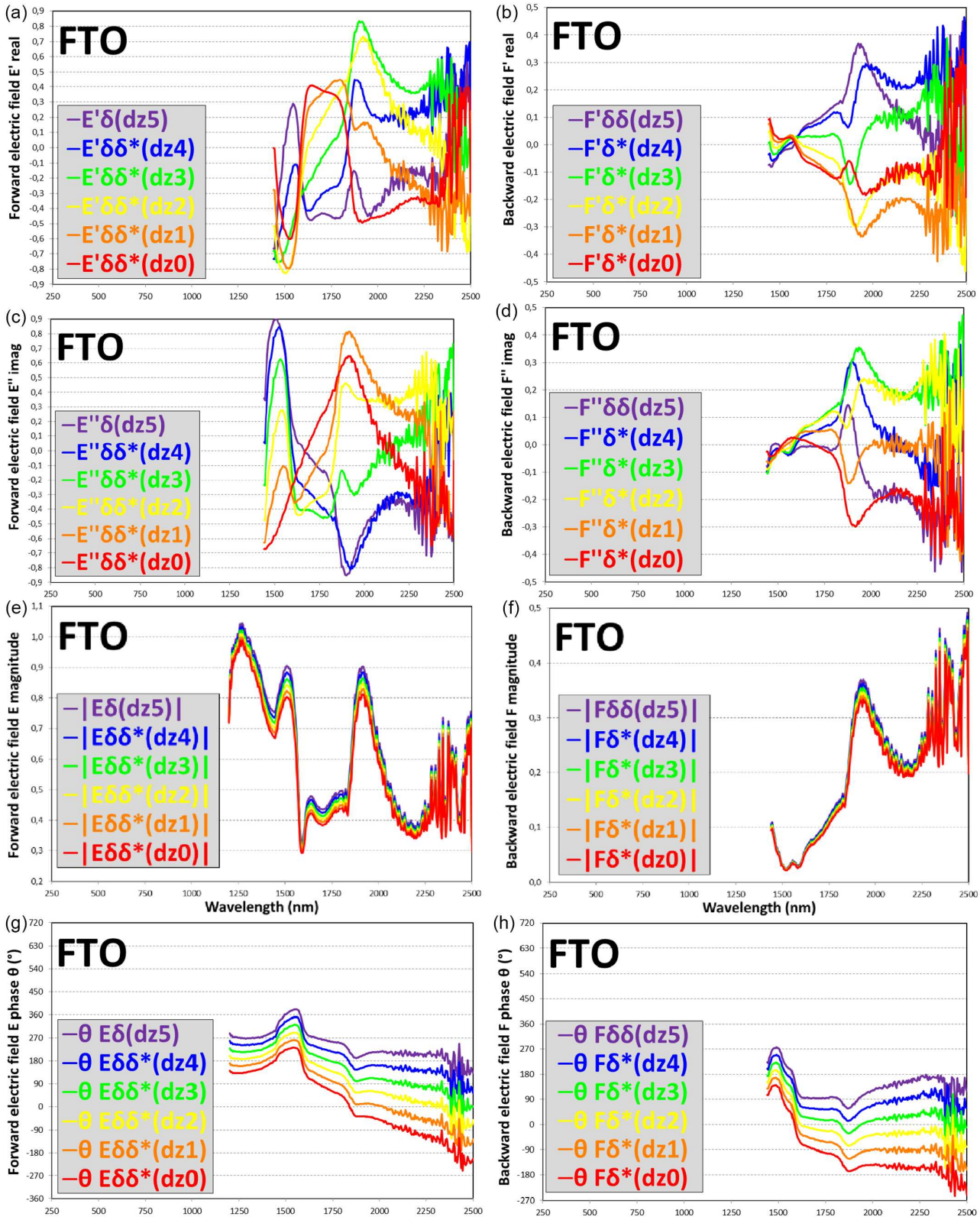

**Figure 9**
**for&back CEF-TGPs (E and F) of FTO for LWRSS$^{FTO}$. Re&Im-P: (a), (b), (c), and (d). Magnitude and phase: (e), (f), (g), and (h)**

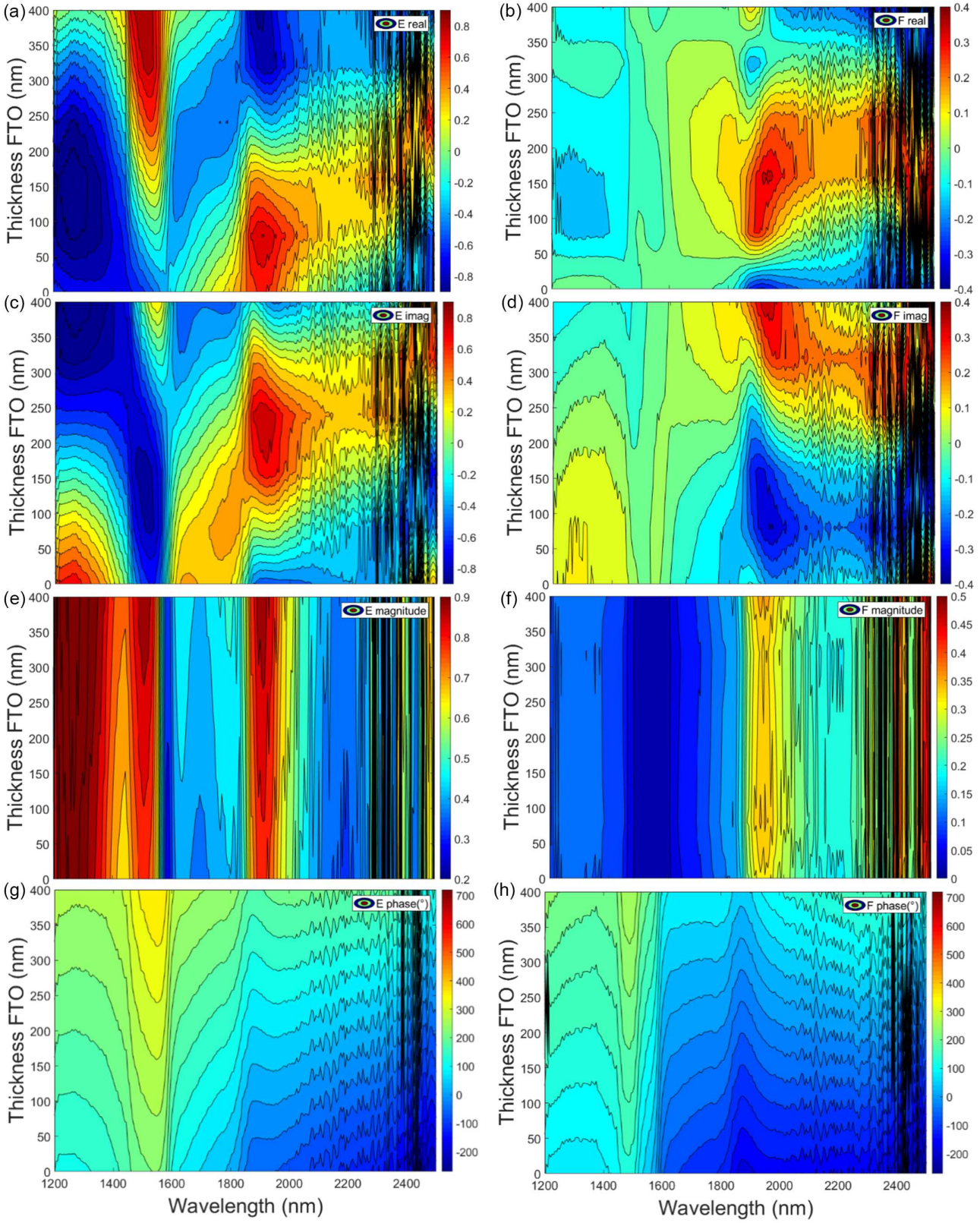

**Figure 10**
**Imaginary parts versus real parts or Nyquist WDD plots for forward E (left) and backward F (right) CEF inside the $WO_3$ film layer**

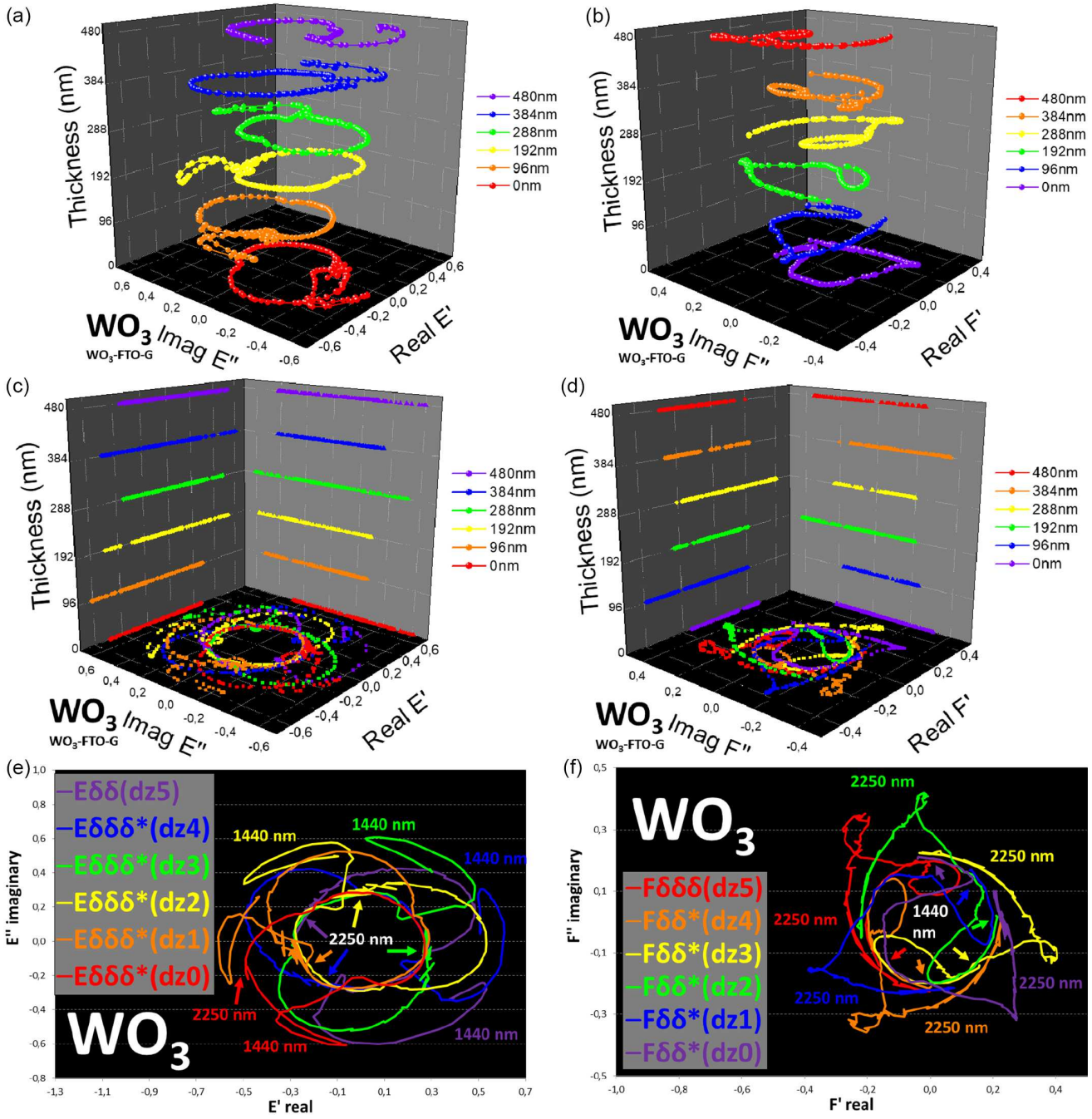

**Figure 11**
**Imaginary parts versus real parts or Nyquist WDD plots for forward E (left) and backward F (right) CEF inside the FTO film layer of the $WO_3$–FTO–G sample**

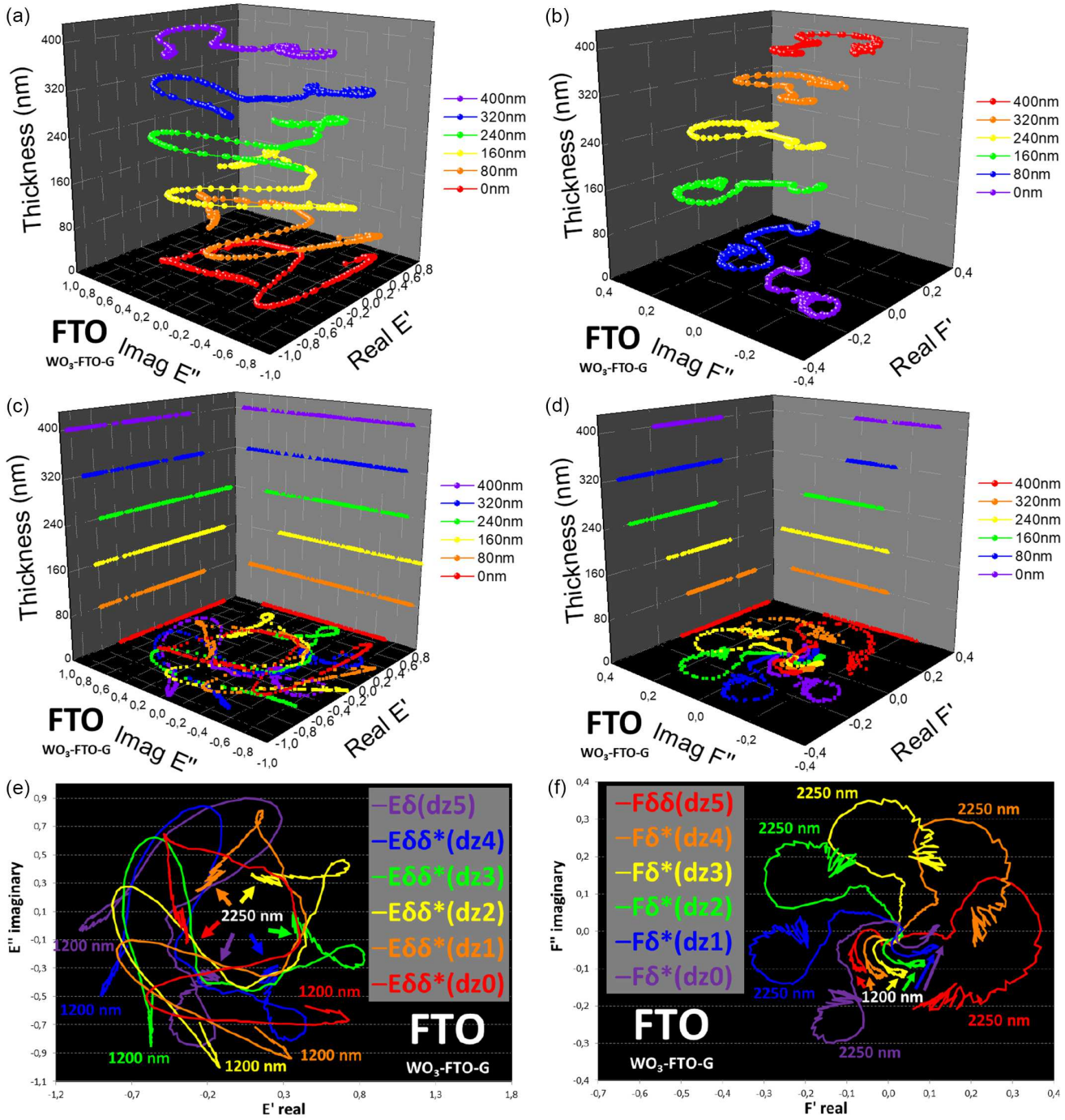

**Figure 12**
**Imaginary parts versus real parts or Nyquist WDD plots for forward E (left) and backward F (right) CEF inside the FTO film layer of the FTO–G sample**

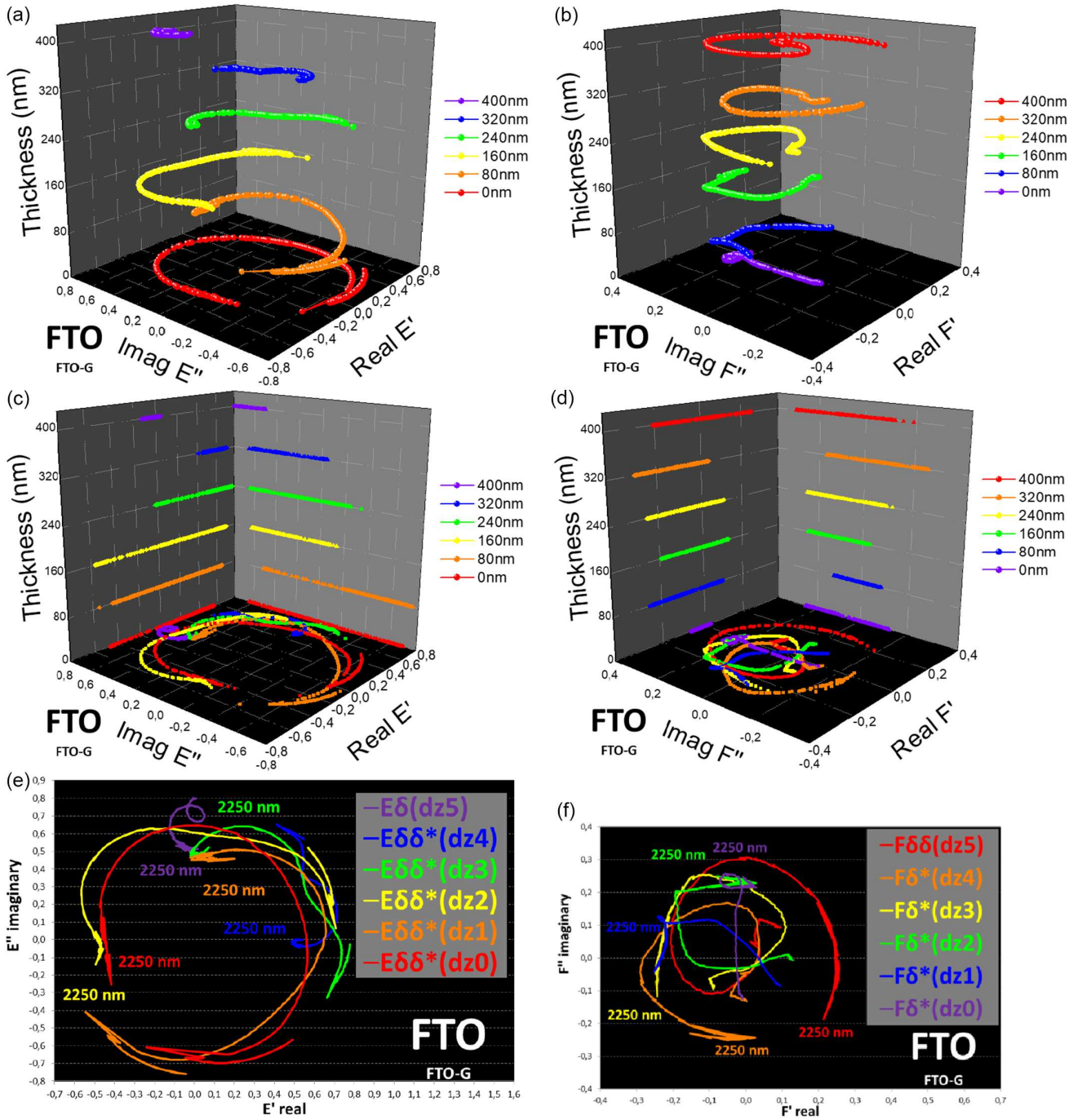

## 5. Conclusion

This work with a three-layer $WO_3$–FTO–G sample is the continuation of a previous work by Barrios-Puerto [33] with the bilayer FTO–G sample. The lower value of $\kappa$ for $WO_3$ than for FTO is responsible for the observed thickness independence of magnitude for the $WO_3$. The present study is intended to establish a solid and consistent optical framework for the determination of intrinsic and extrinsic S&A coefficients within both the 2FM and 4FM. Building on the identification of the EOCs and the SLOBFS, this approach will be extended to FTO–G and G–FTO configurations, as well as to $WO_3$–FTO–G and G–FTO–$WO_3$ samples, by exploiting optical measurements performed on the same sample in both orientations. Future work will also address $WO_3$ layers with thicknesses of 240 nm and 120 nm in order to determine their corresponding SLOBFS values. In addition, analogous analyses will be carried out for NiO–FTO–G samples, enabling a systematic comparison of the optical parameters of $WO_3$ and NiO layers in both BOOS and COOS of ECDs. In summary, the present results demonstrate that the identification of the SLOBFS and the fulfillment of the 3εMR provide a consistent and reproducible criterion to distinguish between substrate- and film-like optical behavior, enabling a unified description of the transition between incoherent and coherent optical regimes in multilayer systems, with direct implications for the analysis and design of complex thin-film structures. The observed relation $\lambda \approx 3d$ for the SLOBFS is reported here as an empirical result derived from the experimental fitting and 3εMR condition.

Building on the present analysis performed for collimated LFs and CEFs, future work will extend this methodology to total and diffuse contributions. In particular, TGPs of total and diffuse LFs will be addressed in the SWRSS, whereas Bode WDDs (magnitude, phase, real, and imaginary components) and Nyquist WDDs (imaginary versus real) derived from total and diffuse CEFs will be explored in the LWRSS. These analyses will be carried out for the FTO layer of the FTO–G sample, as well as for both the FTO and $WO_3$ layers of the $WO_3$–FTO–G sample, considering both sample orientations (FTO–G and G–FTO; $WO_3$–FTO–G and G–FTO–$WO_3$). In addition, the study of two further $WO_3$–FTO–G samples with $WO_3$ thicknesses of 240 nm and 120 nm, instead of 480 nm, together with a NiO–FTO–G sample with a 120 nm NiO layer, will enable the determination of the corresponding SLOBFS values, expected at approximately 720 nm for the 240 nm $WO_3$ layer and at 360 nm for the 120 nm $WO_3$ layer. Initially, the analysis will be restricted to the BOOS.

Extension to both BOOS and COOS for the $WO_3$ and NiO layers considered separately will require optical T&R measurements of the ECD11, ECD12, ECD21, and ECD22 devices in both orientations, which were not available in the recent study by Barrios [32]. Consequently, the fabrication and optical characterization of new ECDs will be required to achieve this objective. Although the FTO layer thickness remains unchanged, its internal collimated CEFs exhibit markedly different complex trajectories when embedded in the $WO_3$–FTO–G system, evidencing the strong influence of multilayer boundary conditions. For completeness, corrected optical Nyquist representations of the collimated electric fields within the FTO layer have also been shown, allowing a direct comparison between bare FTO–G and $WO_3$-coated FTO–G systems. Using the corrected field formalism, the presence of the $WO_3$ overlayer modifies the complex trajectory of the collimated CEF inside the FTO, even though the macroscopic T&R spectra remain nearly unchanged.

Finally, a comparative analysis using non-compressed wavelength will be carried out for $WO_3$ layers of 120 nm and 240 nm in order to assess the robustness of the extracted EOCs and verify their expected independence with respect to layer thickness.

Overall, the present work establishes a consistent and experimentally validated framework for the determination of effective optical constants and for the identification of the transition between coherent and incoherent regimes in multilayer systems, providing a solid basis for the optical analysis of complex thin-film structures.

## Recommendations

The reader is referred to reference [33] for the analysis of the FTO–G bilayer system, which provides the direct experimental and methodological basis extended in the present work to the $WO_3$–FTO–G trilayer configuration.

## Acknowledgments

The author is grateful to the Laboratory for Spectroscopy of Materials of the National Institute of Chemistry of Ljubljana for providing the $WO_3$FTOG sample and the used spectrometer required for measurements and to the mobility grants of Universidad Carlos III de Madrid for supporting research in Slovenia.

## Ethical Statement

This study does not contain any studies with human or animal subjects performed by the author.

## Conflicts of Interest

The author declares that he has no conflicts of interest to this work.

## Data Availability Statement

Data sharing is not applicable to this article as no new data were created or analyzed in this study.

## Author Contribution Statement

**David Barrios-Puerto:** Conceptualization, Methodology, Validation, Investigation, Resources, Data curation, Writing – original draft, Writing – review & editing, Visualization, Supervision, Project administration.

## References

[1] Pfrommer, P., Lomas, K. J., Seale, C., & Kupke, C. (1995). The radiation transfer through coated and tinted glazing. *Solar Energy*, *54*(5), 287–299. https://doi.org/10.1016/0038-092X(94)00132-W

[2] Bohren, C. F., & Huffman, D. R. (1983). *Absorption and scattering of light by small particles*. USA: Wiley.

[3] Kubelka, P. (1948). New contributions to the optics of intensely light-scattering materials. Part I. *Journal of the Optical Society of America*, *38*(5), 448–457. https://doi.org/10.1364/JOSA.38.000448

[4] Beasley, K., Atkins, J. T., & Jr., F. W, Billmeyer. (1967). Scattering and absorption of light in turbid media. In *2nd*

*Interdisciplinary Conference on Electromagnetic Scattering*, 765–784.

[5] Maheu, B., Letoulouzan, J. N., & Gouesbet, G. (1984). Four-flux models to solve the scattering transfer equation in terms of Lorenz–Mie parameters. *Applied Optics*, *23*(19), 3353–3362. https://doi.org/10.1364/AO.23.003353

[6] Barrios Puerto, D. (2024). Intrinsic and extrinsic scattering and absorption coefficients new equations in four-flux and two-flux models used for determining light intensity gradients. *Journal of Optics and Photonics Research*, *1*(3), 131–144. https://doi.org/10.47852/bonviewJOPR42022261

[7] Toral-Lopez, A., Pérez, M. M., Rodríguez-Águila, A. B., Cardona, J. C., Ionescu, A. M., & Godoy, A. (2023). Investigation of the optical properties of indium tin oxide thin films by double integrating sphere combined with the numerical IAD method. *Materials*, *16*(4), 1425. https://doi.org/10.3390/ma16041425

[8] Dvořák, J., Vohánka, J., Buršíková, V., Franta, D., & Ohlídal, I. (2023). Optical characterization of inhomogeneous thin films deposited onto non-absorbing substrates. *Coatings*, *13*(5), 873. https://doi.org/10.3390/coatings13050873

[9] Nosidlak, N., Jaglarz, J., Vallati, A., Dulian, P., Jurzecka-Szymacha, M., Gierałtowska, S., . . . , & Łojewski, T. (2023). The optical properties of thin film alloys of ZnO, $TiO_2$ and $ZrO_2$ with $Al2O_3$ synthesised using atomic layer deposition. *Coatings*, *13*(*11*), 1872. https://doi.org/10.3390/coatings13111872

[10] Adnan, M., Jamil, M. I., Ramzan, B., Hussain, T., Ahmad, A., & Ghani, M. U. (2025). Determination of the optical properties of tungsten trioxide thin film using the transfer matrix method. *Indian Journal of Physics*, *99*(5), 1645–1649. https://doi.org/10.1007/s12648-024-03401-2

[11] Ren, Y., Kong, D., Tan, W., Wang, J., Chen, T., Zhang, Q., . . . , & Xia, W. (2024). Simultaneous determination of the scattering and absorption coefficients of turbid media based on Mueller matrix. *Journal of Modern Optics*, *71*(10-12), 354–363. https://doi.org/10.1080/09500340.2024.2422905

[12] Bilokur, M., & Jonsson, J. C. (2025). Comparing optical four-flux model results with experimental data obtained by integrating sphere measurements. *Applied Optics*, *64*(8), 1918–1923. https://doi.org/10.1364/AO.558629

[13] Stenzel, O., & Wilbrandt, S. (2025). Theoretical aspects of thin film optical spectra: Underlying models, model restrictions and inadequacies, algorithms, and challenges. *Applied Sciences*, *15*(4), 2187. https://doi.org/10.3390/app15042187

[14] Ballester, M., Marquez, E., Bass, J., Würsch, C., Willomitzer, F., & Katsaggelos, A. K. (2025). Review and novel formulae for transmittance and reflectance of wedged thin films on absorbing substrates. *Measurement Science and Technology*, *36*(2), 025502. https://doi.org/10.1088/1361-6501/ada305

[15] Křepelka, J. (2023). *Exact solution of maximally flat antireflection coatings for coherent and incoherent light*. *arXiv Preprint: 2308.02516*

[16] Shklyaev, A. A., Utkin, D. E., Zheng, Z., & Tsarev, A. V. (2023). Redirecting incident light with Mie resonance-based coatings. *Photonics*, *10*(11), 1286. https://doi.org/10.3390/photonics10111286

[17] Isoe, W. M., Mageto, M. J., Maghanga, C. M., Mwamburi, M. M., & Odari, B. V. (2023). Optical modelling of TCO based FTO/$TiO_2$ multilayer thin films and simulation in hydrogenated amorphous silicon solar cell. *Scientific African*, *20*, e01678. https://doi.org/10.1016/j.sciaf.2023.e01678

[18] Niklasson, G. A., & Granqvist, C. G. (2007). Electrochromics for smart windows: Thin films of tungsten oxide and nickel oxide, and devices based on these. *Journal of Materials Chemistry*, *17*(2), 127–156. https://doi.org/10.1039/B612174H

[19] Tan, F., Zhou, J., Guo, Z., Zhang, C., Yu, S., Yang, Y., . . . , & Li, L. (2025). Research progress on electrochromic properties of $WO_3$ thin films. *Coatings*, *15*(11), 1310. https://doi.org/10.3390/coatings15111310

[20] Mak, A. K., Tuna, Ö., Sezgin, N., Üstün, A. M., Yılmaz, Ş., Öztürk, O., & Karabulut, M. (2022). Effect of Al doping on the electrochromic properties of WO3 thin films. *Thin Solid Films*, *751*, 139241. https://doi.org/10.1016/j.tsf.2022.139241

[21] Krüger, L. U., Cholant, C. M., Rodrigues, M. P., Gomez, J. A., Landarin, D. M., Lucio, C. S., . . . , & Avellaneda, C. O. (2022). Photochromism of doped and undoped WO3 sol-gel films: Determination and analysis of optical constants. *Optical Materials*, *128*, 112357. https://doi.org/10.1016/j.optmat.2022.112357

[22] Chen, H., Zhang, L., Guo, P., Zhao, M., Chen, Z., & Ma, H. (2023). Enhanced electrochromic and mechanical properties of WO3 film by substrate effect. *Surfaces and Interfaces*, *41*, 103119. https://doi.org/10.1016/j.surfin.2023.103119

[23] Song, K., Weng, S., Zhou, J., Jiang, R., Cao, H., & Zhang, H. (2023). Tunable optical constants of aluminum tungsten bronzes in electrochromic tungsten oxide thin films. *The Journal of Physical Chemistry C*, *127*(36), 18036–18042. https://doi.org/10.1021/acs.jpcc.3c03521

[24] Nur Ozer, Z., Ozkan, M., & Pat, S. (2024). Investigation of the microstructural, surface, and optical properties of WO3-doped ZnO thin films. *Inorganic Chemistry Communications*, *170*, 113301. https://doi.org/10.1016/j.inoche.2024.113301

[25] Zheng, J. Y., Sun, Q., Yang, H., Yu, S., Li, M., Yu, X., . . . , & Li, S. (2024). Amorphous bismuth and GO co-doped WO3 electrochromic film with fast-switching time and long-term stability. *Dalton Transactions*, *53*(6), 2460–2464. https://doi.org/10.1039/D3DT03805J

[26] Wang, Z., Liu, G., Li, C., Qiao, M., Tian, M., Lin, X., . . . , & Xu, S. (2025). W/$WO_3$/$TiO_2$ multilayer film with elevated electrochromic and capacitive properties. *Materials*, *18*(1), 161. https://doi.org/10.3390/ma18010161

[27] Nakrela, A., Nehal, M. E. F., Bouzidi, A., Miloua, R., Medles, M., Khadraoui, M., & Desfeux, R. (2025). Comprehensive investigation of WO3-x thin films: Structural, optical, and electrical insights, with application in photodegradation of dyes. *Ceramics International*, *51*(13), 16997–17006. https://doi.org/10.1016/j.ceramint.2025.02.009

[28] Nie, S., Lian, Y., Han, H., Zhao, L., & Liu, Z. (2025). Efficient electrochromic electrode materials based on $WO_3$/$Ni(OH)_2$ with dual ion implantation modulability and energy level matching. *Advanced Materials Technologies*, *10*(9), 2401295. https://doi.org/10.1002/admt.202401295

[29] Kwon, S.-J., Rajesh, J. A., Kang, S., & Ahn, K. (2026). Electrochemical and optical characterization of $WO_3$ films synthesized by pulse current method and their application in electrochromic devices. *Electrochimica Acta*, *549*, 148076. https://doi.org/10.1016/j.electacta.2025.148076

[30] Sharma, R., Nihal, Sharma., M, & Goswamy, J. K. (2026). Investigation of electrochromic properties of $MoSe_2$/$WO_3$ nanocomposite. *Materials Letters*, *406*, 139968. https://doi.org/10.1016/j.matlet.2025.139968

[31] Čolović, M., Jerman, I., Gaberšček, M., & Orel, B. (2011). POSS based ionic liquid as an electrolyte for hybrid electrochromic devices. *Solar Energy Materials and Solar Cells*, *95*(12), 3472–3481. https://doi.org/10.1016/j.solmat.2011.08.009

[32] Barrios, D. (2026). Parameters of differential equations in four-flux and two-flux models approximated for $WO_3$ - NiO inorganic electrochromic devices. *Journal of Quantitative Spectroscopy and Radiative Transfer*, *348*, 109718. https://doi.org/10.1016/j.jqsrt.2025.109718

[33] Barrios-Puerto, D. (2025). Spectral limit of the optical behavior between film and substrate for a fluorine-doped tin oxide (FTO) transparent conductive layer. *Journal of Optics and Photonics Research. Advance online publication*. https://doi.org/10.47852/bonviewJOPR52025408

[34] Osiac, M., Dumitru, M., Ion, V., & Tirca, I. (2025). Structure and optical property relationship in $WO_3$ thin films fabricated by PLD. *Physica B: Condensed Matter*, *718*, 417844. https://doi.org/10.1016/j.physb.2025.417844

[35] Nwifior, K. (2024). Refractive index of tungsten oxide nanostructured thin films grown at room temperature by chemical bath deposition method for optical gas sensing. *Ebonyi State College of Education, Ikwo Journal of Educational Research*, *10*(1), 1–8.

**How to Cite:** Barrios-Puerto, D. (2026). Film and Substrate Spectral Optical Behaviors of a Tungsten Trioxide ($WO_3$) Thin Layer Deposited on Fluorine-Doped Tin Oxide (FTO)–Coated Glass. *Journal of Optics and Photonics Research*. https://doi.org/10.47852/bonviewJOPR62029118

## Appendix

| Nomenclature | |
|---|---|
| Greek symbols | |
| $\delta$ | z coordinate at top inner interface between FTO and glass layers |
| $\delta\delta$ | z coordinate at top inner interface between $WO_3$ and FTO layers |
| $\delta\delta\delta$ | z coordinate at top outer interface |
| $\varepsilon$ | extinction coefficient |
| $\varepsilon^{\kappa n}$ | $\varepsilon$ obtained from optical constants |
| $\varepsilon^{i}$ | $\varepsilon$ obtained from forward CDE |
| $\varepsilon^{j}$ | $\varepsilon$ obtained from backward CDE |
| $\kappa$ | imaginary part of complex refractive index |
| $\lambda$ | wavelength |
| $\tau$ | Fresnel transmission coefficient |
| $\tau^{S}$ | $\tau$ for S polarization |
| $\tau^{P}$ | $\tau$ for P polarization |
| $\rho$ | Fresnel reflection coefficient |
| $\rho^{S}$ | $\rho$ for S polarization |
| $\rho^{P}$ | $\rho$ for P polarization |
| English Symbols | |
| 0 | z coordinate at bottom interface |
| 2FM | two-flux model |
| 3εMR | three-extinction matching requirement |
| 4FM | four-flux model |
| BOOS | bleached-off optical state |
| cc | collimated-collimated suffix for 4FM calculated T and R |
| CEF | complex electric field |
| CDE | collimated differential equation |
| COOS | colored-on optical state |
| dz | thickness of a layer |
| DDE | diffuse differential equation |
| E | forward electric field |
| ECD | electrochromic device |
| F | backward electric field |
| for&back | forward and backward |
| FTO | fluorine-doped indium oxide |
| FTOG | bilayer FTO-glass sample |
| G | glass |
| GEG | glass–electrolyte–glass |
| i | forward light sense |
| I | collimated forward light flux |
| $I^{0}$ | I at bottom interface |
| $I^{\delta}$ | I at top inner interface between FTO and glass layers |
| $I^{\delta\delta}$ | I at top inner interface between $WO_3$ and FTO layers |
| $I^{\delta\delta\delta}$ | I at top outer interface |

(*Continued*)

(*Continued*)

| Nomenclature | |
|---|---|
| j | backward light sense |
| J | collimated backward light flux |
| $J^0$ | J at bottom interface |
| $J^{\delta}$ | J at top inner interface between FTO and glass layers |
| $J^{\delta\delta}$ | J at top inner interface between $WO_3$ and FTO layers |
| $J^{\delta\delta\delta}$ | J at top outer interface |
| LF | light flux |
| LWRSS | longer wavelength range of the solar spectrum |
| $M_{oi}$ | interface matrix between medium outside "o" and inside "i" mediums |
| $N_s$ | substrate "s" layer matrix |
| n | real part of complex refractive index |
| n' | complex refractive index |
| R | reflectance |
| r | collimated interface reflectance |
| $r_{oWO3FTOG}$ | collimated reflectance of $WO_3$ and FTO layers from outside air to glass |
| $r_{GFTOWO3o}$ | collimated reflectance of $WO_3$ and FTO layers from glass to outside air |
| $R_{cc}$ | calculated specular reflectance |
| $R_{spe}$ | measured specular reflectance |
| Re&Im-P | real and imaginary parts |
| S&A | scattering and absorption |
| SWRSS | shorter wavelength range of the solar spectrum |
| T | transmittance |
| t | collimated interface transmittance |
| TGP | thickness gradient plot |
| $t_{oWO3FTOG}$ | collimated transmittance of $WO_3$ and FTO layers from outside air to glass |
| $t_{GFTOWO3o}$ | collimated transmittance of $WO_3$ and FTO layers from glass to outside air |
| $T_{cc}$ | calculated regular transmittance |
| $T_{reg}$ | measured regular transmittance |
| TSLSS | three substrate layers sandwich structure |
| WRSS | wavelength range of the solar spectrum |
| WDD | wavelength-dependent diagram |